Ore Geology Reviews 121 (2020) 103475

Contents lists available at ScienceDirect

Ore Geology Reviews

journal homepage: www.elsevier.com/locate/oregeorev

The state of Au and As in pyrite studied by X-ray absorption spectroscopy of natural minerals and synthetic phases

Olga N. Filimonova[a], Boris R. Tagirov[a,*], Alexander L. Trigub[b], Maximilian S. Nickolsky[a], Mauro Rovezzi[c], Elena V. Belogub[d], Vladimir L. Reukov[a], Ilya V. Vikentyev[a]

[a] Institute of Geology of Ore Deposits, Petrography, Mineralogy and Geochemistry (IGEM RAS), 35, Staromonetny per., 119017 Moscow, Russia
[b] National Research Centre "Kurchatov Institute", 1, Akademika Kurchatova pl., 123182 Moscow, Russia
[c] Université Grenoble Alpes, CNRS, IRD, Irstea, Météo France, OSUG, FAME, 38000 Grenoble, France
[d] South Ural Federal Scientific Center of Mineralogy and Geoecology, Urals Branch of RAS, Chelyabinsk District, 456317 Miass, Russia

ARTICLE INFO

Keywords:
Invisible gold
Arsenic
Pyrite
Synthetic minerals
Hydrothermal ore deposits
X-ray absorption spectroscopy

ABSTRACT

In many hydrothermal deposits arsenian pyrite contains economic concentrations of Au in an "invisible" form, which is structurally bound in pyrite or has grain size < 0.1 μm. Here we use X-ray absorption spectroscopy (XAS) of natural minerals and synthetic phases to reveal the forms of Au occurrence in pyrite and determine the effect of physicochemical-compositional parameters on the concentration and state of "invisible" Au. A sample of natural arsenian pyrite with 300 ppm Au and 0.34 wt% As (average value) from the Samolazovskoe Au-sulfide deposit (Yakutia, Russia) was used to study the states of Au and As, and two arsenian pyrite samples from the Vorontsovka Carlin-type deposit (North Urals, Russia) were used to characterize the state of As. The synthesis experiments were performed employing the hydrothermal method at 300 °C/P_{sat} and 450 °C/1000 bar, at contrasting redox states – in oxidized (H_2S/H_2SO_4 redox buffer) and reduced (H_2S predominates) fluids, in As-free and As-bearing systems. As a result, a series of samples of As-free and arsenian pyrites was obtained with Au concentrations from ca. 100 to 300 ppm. The concentration of "invisible" Au, which was homogeneously distributed within the samples, was independent of As concentration but decreased with increasing synthesis temperature. The concentration of Au dissolved in acidic sulfide hydrothermal fluid was not affected by the presence of As. The X-ray absorption XANES/EXAFS spectra were recorded simultaneously at Au L_3-edge and As K-edge. The use of the high energy resolution fluorescence detection (HERFD-XAS) mode made possible to acquire data for the trace amounts of Au in As-rich samples. According to XANES spectroscopy Au occurs in pyrite in the 1 + oxidation state. Two forms of Au were detected in the pyrite samples: the solid solution Au and Au_2S-like clusters/inclusions. In the solid solution state Au replaces Fe in the structure of pyrite and is coordinated only with sulfur atoms (N_S = 6, $R_{Au\text{-}S}$ = 2.41 ± 0.01 Å) in all pyrite samples independently of the conditions of their formation/synthesis and As content, no As atoms were detected in the local atomic environment of Au. Thus, the Au-S distance in the 1st coordination shell increased by 0.15 Å relatively to the Fe-S distance in pure pyrite. The distant coordination shells of the solid solution Au correspond to the pyrite crystal structure. The presence of the Au_2S-like clusters leads to a significant decrease of the calculated values of coordination number of Au and Au-S interatomic distance. In natural pyrite samples from the Vorontsovka deposit As^{1-} replaces S in the anionic sites, increasing the 1st shell As-S and As-Fe distances by 0.07–0.1 Å relatively to the pure pyrite structure. A contribution of As^{3+} oxide was detected in pyrite from the Vorontsovka deposit. The synthetic pyrite samples contain As in the form of As^{1-} solid solution and As^{3+} and As^{5+} oxides. Results of our study show that neither the concentration and speciation of As nor the redox state of the system affect the state of "invisible" Au in the studied pyrites.

1. Introduction

Gold in hydrothermal ore deposits is often associated with As-bearing minerals – arsenian pyrite FeS_2, arsenopyrite FeAsS, and löllingite $FeAs_2$. Arsenian pyrite is among the main ore minerals in many types of hydrothermal deposits, including the world-class ones

* Corresponding author.
E-mail address: boris1t@yandex.ru (B.R. Tagirov).

https://doi.org/10.1016/j.oregeorev.2020.103475
Received 31 August 2019; Received in revised form 3 March 2020; Accepted 15 March 2020
Available online 17 March 2020

where Au is extracted as the main ore component or byproduct: sediment-hosted (in particular, Carlin-type) Au deposits (see, for example, Palenik et al., 2004, and references cited; Large et al., 2009), orogenic Au deposits (Groves et al., 1998; Goldfarb et al., 2005; Palenova et al., 2015), epithermal (Pals et al., 2003; Cook et al., 2009), mesothermal deposits (Genkin et al., 1998), volcanogenic massive sulfide (VMS) deposits (Vikentyev, 2006; Wagner et al., 2007; Mercier-Langevin et al., 2011). In these deposits, Au-bearing sulfides often contain dominant portion of Au in an "invisible" (submicroscopic) state, which cannot be identified by conventional optical or scanning electron microscopes. The "invisible" Au exists either in the form of nanoscale particles or as the solid solution Au (Fleet and Mumin, 1997; Deditius et al., 2014). Extraction of Au from sulfide ores and concentrates is often associated with substantial Au losses when "invisible" form of Au predominates in the ore. Therefore, the problem of "invisible" Au has important implications for the mining of Au-bearing ores and mineral processing industry.

In many types of hydrothermal ores there is a positive correlation between the concentrations of Au and As in pyrite (e.g., Reich et al., 2005; Deditius et al., 2014), but many deposits without the distinct correlation between Au and As are also known. For example, no correlation between Au and As in pyrite occurs in the ores of the shear-hosted gold-vein system of the Fairview mine, South Africa (Fleet et al., 1993), VMS La Zarza, Migollas and Sotiel deposits, the Iberian Pyrite Belt (Leistel et al., 1997), multistage sedimentary-metamorphic (orogenic) sediment-hosted giant Sukhoi Log gold deposit (Fig. 9 in Large et al., 2007), "orogenic" gold deposits of the northern margin of the North China Craton, China (Cook et al., 2009), intrusion-related lode gold deposits of the Xiaoqinling-Dabie Orogenic Belt, China (Bi et al., 2011), sediment-hosted (siltstone, shale, and limestone) Qiuling gold deposit in the West Qinling orogenic belt, China (Fig. 4 in Chen et al., 2015), Agua Rica Cu (Mo-Au) porphyry high-sulfidation epithermal deposit, Argentina (Fig. 5 in Franchini et al., 2015). No significant correlation between Au and As in pyrite was observed in the ores of Au-bearing deposits of the Urals (Russia), including VMS deposits (Vikentyev, 2015; Tseluyko et al., 2019), the Petropavlovsk Au-porphyry deposit (Vikentyev et al., 2017), the Novogodnee-Monto Fe-Au skarn deposit (Ivanova et al., 2015), and the Svetlinsk Au-Te deposit (Vikent'eva and Bortnikov, 2015). Binary diagrams show low correlation between Au and As in pyrite of the Zn-Pb-Se-Bi-Au-rich VMS Falun deposit, Sweden (Fig. 9 in Kampmann et al., 2018).

The way As affects the concentration of Au in arsenian pyrite is still unknown. It is generally accepted that these elements can substitute for Fe (Au) and S (As) in the structure of pyrite. The positive correlation between the concentrations of Au and As implies that the presence of As promotes the incorporation of Au into the cationic sites of pyrite (c.f., Reich et al., 2005; Chen et al., 2013). However, the experiments on the adsorption of Au on the surface of pyrite (Widler and Seward, 2002), and on the synthesis of Au-bearing As-free pyrites (Kozerenko et al., 2001; Laptev and Rozov, 2006; Trigub et al., 2017a, Pokrovski et al., 2019) showed that high, up to a few hundred ppm, concentrations of Au can be coprecipitated in the "chemically bound" form with the As-free pyrite. The latter data questioned the role of As in the formation of the solid solution Au in pyrite via the charge compensation scheme.

The state of Au and As, including their local atomic environment, position in the pyrite structure in the case of solid solution, and valence state can be reliably determined only by spectroscopic methods, among which the X-ray absorption spectroscopy (XAS) is the most informative at the present. In the previous studies we used XAS in order to investigate the state of Au in covellite CuS (Tagirov et al., 2016), in the minerals of the Fe-As-S system (Trigub et al., 2017a), and in sphalerite (Zn,Fe)S (Filimonova et al., 2019). In these studies, we applied the high energy resolution fluorescence detection spectroscopic technique (HERFD-XAS, Glatzel and Bergman, 2005). This method allows to acquire Au L_3-edge spectra from the As-bearing phases, whereas the use of the conventional partial fluorescence yield (PFY) mode for this purpose is impossible due to the limited energy resolution of the solid state detector – ~150 eV at Mn $K\alpha$, the weak signal of the $L\alpha$ line from the trace amount of "invisible" Au is masked by the As $K\alpha$ fluorescence (Trigub et al., 2017a). Another advantage of HERFD technique is that the weak features of Au(I) spectra are considerably enhanced compared with the PFY spectra, which facilitates interpretation and modeling (c.f., Tagirov et al., 2016). Previously, we determined the state of "invisible" Au in the samples of As-free pyrite (Trigub et al., 2017a) by means of X-ray absorption near edge structure (XANES) and extended X-ray absorption fine structure (EXAFS) spectroscopies. We found that Au substitutes for Fe in the pyrite structure. Similar parameters of the local atomic environment of Au in natural arsenian pyrite were determined by Merkulova et al. (2019) employing HERFD-XAS method. Despite the presence of As, only S atoms were found by the authors in the vicinity of Au. At the same time, Pokrovski et al. (2019) analyzed the XANES spectra of Au in the As-free pyrites and suggested that, instead of the formation of the solid solution, Au in pyrite presents mainly as "(poly)sulfide clusters composed on S-Au-S linear units, similar to those in aqueous complexes". Thus, the controversial interpretations of the results of XAS experiments make a conclusive determination of the state of Au in pyrite unfeasible.

The major goal of the present study is to determine unambiguously the state of Au in pyrite and elucidate the effect of the physicochemical-compositional parameters on the forms of occurrence of Au. For this purpose, we introduced Au into synthetic As-free and As-bearing pyrites and studied the synthesized samples by means of XAS. The synthesis experiments were performed employing the hydrothermal method in the wide range of temperatures/pressures (300 °C/P_{sat} – 450 °C/1 kbar), redox states (from oxidized to reduced sulfide fluids), and As concentrations (from As-free to As-bearing pyrites with up to 1.5 wt% As). The data on the states of Au and As in the synthetic samples were compared to those of the natural arsenian Au-bearing pyrite from the Samolazovskoe Au-sulfide deposit (Yakutia, Russia). The state of As was determined in the samples of synthetic and natural Au-bearing pyrites, including samples from the Vorontsovka Carlin-type deposit (North Urals, Russia). As a result of the interpretation of XAS data, the different forms of Au were identified in pyrite, among which the solid solution Au was the dominant one. Results of our work show that the chemistry of Au and As in ore-forming systems can be decoupled: the presence of As and its speciation does not affect the concentration and state of "invisible" Au in pyrite.

2. Materials and methods

2.1. Method of synthesis

The hydrothermal method was employed to synthesize Au-bearing pyrites. Experiments were carried out at 450 °C/1 kbar and 300 °C/P_{sat} using Ti autoclaves (VT-8 alloy) with an internal volume of ~20 ml. The redox conditions of the experimental system varied from oxidized (450 °C, the sulfide-sulfite couple, produced by the elemental sulfur dissolution and disproportionation, controlled the redox state) to reduced (300 °C, the thioacetamide CH_3CSNH_2 or Al_2S_3 were used as a source of sulfur). Reagent grade chemicals and freshly boiled distilled water cooled under Ar flow were used throughout the synthesis experiments. The starting materials are listed in the 2nd column of Table 1.

In the first experimental series, performed at 450 °C/1 kbar, pyrrhotite $Fe_{0.9}S$ was used as a precursor for the synthesis of pyrite. The conventional solid-state technique was used to synthesize the pyrrhotite powder. The starting chemicals for the pyrrhotite synthesis were powders of Fe and S. Necessary quantities of the reagents were sealed under vacuum in the silica glass tube and kept at 450 °C for 7 days. The phase composition of the synthesized powders was verified using X-ray diffraction (XRD) and corresponded to pyrrhotite. The synthesized pyrrhotite was placed into small Ti container attached to the Ti partition in

Table 1
Starting materials used in pyrite synthesis experiments, solute concentrations, and compositions of synthetic pyrites used in the X-ray absorption spectroscopy experiment.

Sample No.	Starting materials	Solute concentration, mol·(kg H_2O)$^{-1}$ S/As_2O_3	Au in fluid, mol·(kg H_2O)$^{-1}$	Phase composition of synthesis products	Concentration of admixtures (ppm)				
					AAS	LA-ICP-MS			
					As	Au min	Au max	As min	As max
High temperature synthesis (450 °C/1 kbar)									
8	$Fe_{0.9}S$ + S + Au_{cr}	1.1/0	2.3E-6	Pyrite	bdl[1]	75 ± 2	120 ± 3	bdl[1]	
10	$Fe_{0.9}S$ + S_{cr} + As_2O_3 + Au_{cr}	1.1/0.1	1.6E-6	Pyrite	5800 ± 60	78 ± 2	117 ± 3	8100 ± 180	10400 ± 230
16	$Fe_{0.9}S$ + S_{cr} + As_2O_3 + Au_{cr}	1.0/0.39	2.6E-5[3]	Pyrite + As-S amorphous phase (< 5 vol%)	6300 ± 60	88 ± 3	100 ± 2	12900 ± 270	30700 ± 650
6/14[2]	$Fe_{0.9}S$ + S_{cr} + Au_{cr}	1.5/0	5.9E-6	Pyrite	bdl[1]	86 ± 9		bdl[1]	
Low temperature synthesis (300 °C/$P_{sat.}$)									
17/1	FeOHHS·nH_2O (+200 ppm Au) + Thioacetamide	0.53/0/0	not analyzed	Pyrite	bdl[1]	200 ± 5		bdl[1]	
17/2	FeOHHS·nH_2O (+50 ppm Au) + Au_{cr} + Al_2S_3 + As_2O_3	0.49/0/0.008	not analyzed	Pyrite + Arsenopyrite + Löllingite (< 5 vol%)	not analyzed	130 ± 3		49200 ± 1390	62000 ± 1780
5/2	FeOHHS·nH_2O (+50 ppm Au) + Au_{cr} + Al_2S_3 + As_2O_3	0.38/0/0.034	not analyzed	Pyrite + Arsenopyrite (< 5 vol%)	not analyzed	230 ± 5	360 ± 6	24000 ± 590	33500 ± 930

[1]bdl – below detection limit (2σ): AAS – As 200 ppm, LA-ICP-MS – Au 0.7 ppm, As 5 ppm; [2] Trigub et al. (2017a); [3]possible contamination with Au-bearing As_2S_3 amorphous phase.

the upper part of the autoclave. A strip of Au foil was also attached to the partition, avoiding contact with pyrrhotite. The autoclaves were loaded with the necessary amount of S_{cr} (taking into account the reaction of S with $Fe_{0.9}S$ with the formation of pyrite), As_2O_3 when necessary, distilled water, and Ar saturated. Pressure in the autoclaves was controlled by the degree of filling with water. The closed autoclaves were placed into the gradientless furnaces preheated to 450 °C. During the experiment, the temperature was controlled within ± 2 °C using a K-type thermocouple. The duration of the synthesis experiments was 4 weeks. After the experiment the autoclaves were quenched in cold water, the synthesis products were extracted from the containers and dried under vacuum. The details on the method of determination of Au dissolved in the fluid can be found in Trigub et al. (2017b). In brief, the experimental solution was extracted from the autoclaves, next the autoclave walls were three times washed with 5 ml of hot aqua regia. The experimental and washing solutions were collected in the Pyrex glass flasks (one for each experiment) and evaporated to the wet salt state. The residuals were dissolved in 5 ml of aqua regia and again evaporated. Then 10 ml of 2M HCl were added to the flasks. The solutions obtained were analyzed to determine the Au content.

The second series was prepared by means of the modified technique developed by Fadeev and Kozerenko (1999) for the synthesis of Au-bearing pyrite. In this series, Au-bearing hydrotroilite FeOHHS·nH_2O was used as a starting material for the pyrite synthesis. The method consisted of precipitation of Au-bearing $Fe(OH)_3$·mH_2O from the solution of $Fe(NO_3)_3$·$9H_2O$ (C_{Fe} = 1 g/L) which contained $HAuCl_4$. The quantity of $HAuCl_4$ was calculated in the assumption that is was completely coprecipitated with $Fe(OH)_3$·mH_2O. The synthesis experiments were performed in glass flasks of 1 L volume. Precipitation was performed at ambient temperature by slow addition of NH_4OH solution (20%) under stirring until the appearance of the slow smell of ammonia. Then thioacetamide (C_2H_5NS), which was used as a source of sulfur, was dissolved in the solution. The concentration of thioacetamide was calculated to produce hydrotroilite FeOHHS nH_2O from Fe $(OH)_3$ and have the total dissolved sulfur concentration of 0.1 mol/L. The glass flasks were left for several days under stirring to react thioacetamide with $Fe(OH)_3$·mH_2O. The resulted powders were separated from the solution by filtration and washed with distilled water on the filter. Finally, they were loaded into Ti autoclaves together with the source of S (thioacetamide or Al_2S_3) and distilled water. In one experiment As-free Au-bearing pyrite was synthesized from the Au-bearing hydrotroilite powder only. In two other experiments, in addition to hydrotroilite, As_2O_3 and Au metal were loaded to the autoclaves. Conditioning of the solid phases was performed at 300 °C/$P_{sat.}$ The method of the conditioning was similar to the high-temperature experiments.

Gold sulfide Au_2S_{cr} – reference material – is a metastable compound synthesized in several stages by sulfidizing aqueous Au cyanide solution at ambient temperature as described in Tagirov et al. (2006). As-bearing reference materials – arsenopyrite (FeAsS) and löllingite ($FeAs_2$) – were obtained by salt flux method as described in Chareev (2016). Chemical and phase compositions of the reference materials were verified by means of scanning electron microscopy (SEM/EDS) and XRD analysis.

2.2. Samples of natural arsenian pyrites

The Samolazovskoe Au-sulfide deposit is located in the south part of the Central Aldan ore district (Yakutia, Russia). The Au reserves of the deposit are 9260 kg, the average Au grade is 3.5 g/t. The ore bodies of the deposit are localized in syenite intrusion at the contact of syenites and marmorized dolomites and are associated with processes of hydrothermal alteration of syenites and country rocks (Borisenko et al., 2015; Leontiev et al., 2018; Belogub and Novoselov, 2019). The highest Au grade ores were found in the pyrite-quartz-fluorite veins which were formed in the temperature range from 325 to 380 °C (Borisenko et al.,

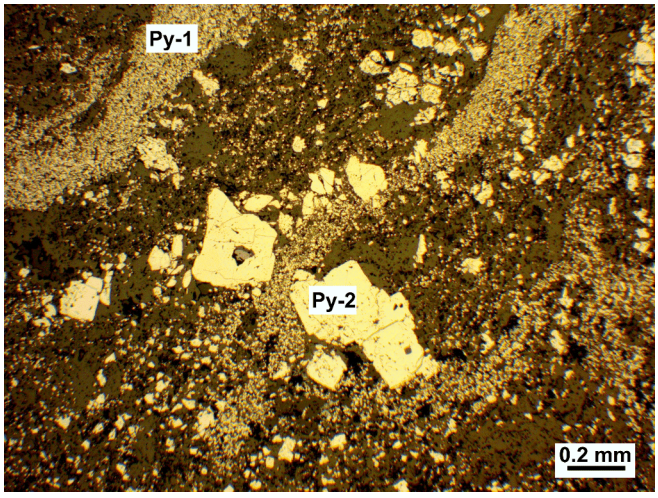

Fig. 1. Fine-grained pyrite mass (Py-1) and subhedral pyrite (Py-2) in the ore of the Samolazovskoe Au-sulfide deposit.

2015). In the present work, we studied Au-rich arsenian pyrites from the veinlet-disseminated Au ore. The ore is located in the roscoelite-carbonate-fluorite-quartz alteration zones in the syenite and contains three types of pyrite: (i) the Au-rich fine-grained pyrite, (ii) subhedral coarse-grained pyrite, and (iii) zoned pyrite grains. The studied sample of pyrite ore contained the type (i) and (ii) pyrites (Fig. 1). The fine-grained Au-rich pyrite of the type (i) was separated from the other minerals of the sample and used for XAS experiment.

The second type of arsenian pyrite was sampled at the Vorontsovka Carlin-type deposit which is located in the Tagil zone of the North Urals (Russia), in the Turya-Auerbakh mineral district. The deposit is one of the largest Au deposits of the Urals. It hosts > 100 t Au in ores with the average Au grade of 7 g/t (Murzin et al., 2017; Vikentyev et al., 2019; Kovalchuk et al., 2019). Late antimony-mercury-thallium-arsenic gold ore bodies of Carlin type, accompanied by quartz-hydromica alteration, are superimposed on the skarn, limestone breccias, and polymetallic quartz-polysulfide mineralization. The Carlin-type sulfide gold-pyrite-realgar mineralization was formed at 370–250 °C. In these ores, subhedral pyrite is associated with arsenopyrite and often is cemented by stibnite and realgar. Since the pyrite samples contain < 10 ppm of Au only As was studied by means of XAS.

2.3. Analytical methods

The morphology of the synthesized minerals was studied by means of SEM/EDS using the JSM-5610LV microscope equipped with Ultim Max 100 energy dispersive spectrometer. Chemical composition of the synthesized and natural minerals was determined via three independent analytical techniques: wet chemistry, electron probe microanalysis (EPMA), laser ablation inductively coupled mass spectrometry (LA-ICP-MS), and atomic absorption spectroscopy (AAS). The EPMA analyses were performed using JEOL JXA-8200 WD/ED combined electron probe microanalyzer equipped with 5 wavelength dispersive X-ray spectrometers. The New Wave 213 laser coupled with the Thermo X Series2 quadrupole ICP-MS was used at IGEM RAS (Moscow) to determine the concentrations of ^{197}Au and ^{75}As. The sulfide reference material MASS-1 (Wilson et al., 2002) and UQAC-FeS-1 (Piña et al., 2016) were used as the calibration standards. The ^{33}S and ^{57}Fe isotopes were used as internal standards. Operating conditions applied for EPMA and LA-ICP-MS analyses are listed in Tables A.1 and A.2, correspondingly.

The Au concentration in aqueous solutions was analyzed using inductively coupled plasma mass spectrometry ICP-MS (X Series 2 Thermo Scientific mass spectrometer). The limit of detection, determined by analysis of blank solutions prepared identically to the samples, was 0.1 ppb, the accuracy of the analyses was ± 10%. The composition of several solid samples was determined using ICP-MS or flame AAS (Varian SpectrAA Duo) methods after decomposition in aqua regia.

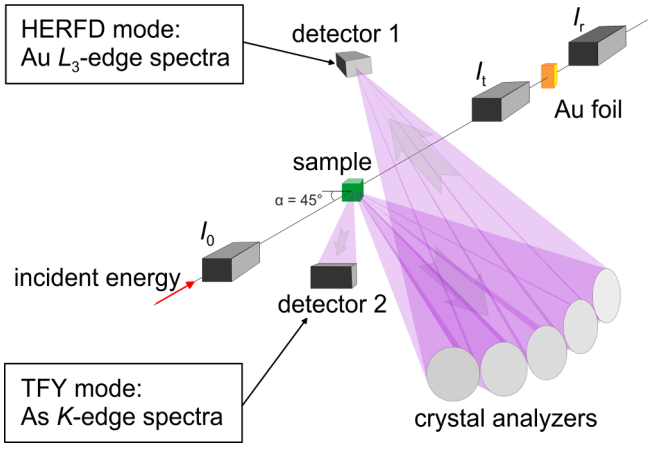

Fig. 2. Schematic overview of the experimental set-up at the BM16–FAME–UHD beamline. The Au L_3-edge spectra were recorded in the high energy resolution fluorescence detection (HERFD) mode using a 5-crystal spectrometer of a Johann-type geometry. Simultaneously the beam intensity was measured with ionization chambers (I_0, I_t, I_f, I_R), and the fluorescence As K-edge spectra was recorded using a photodiode. After the sample, the remaining beam passed through a second ionization chamber (I_t), Au calibration foil, and a third ionization chamber (I_R) before termination.

2.4. X-ray absorption spectroscopy (XAS)

Two series of XAS experiments were performed. The main series consisted of the registration of HERFD-XAS Au L_3-edge and PFY-XAS As K-edge spectra of Au-bearing pyrites at the European Synchrotron Radiation Facility (ESRF, Grenoble, France). The second series of experiments consisted in the registration of PFY-XAS As K-edge spectra of arsenian pyrites from the Vorontsovka deposit and the registration of the spectra of reference substances at Kurchatov Synchrotron Radiation Source (KSRS, Moscow, Russia).

The HERFD-XAS Au L_3-edge and PFY-XAS As K-edge spectra were simultaneously registered at the BM16–FAME–UHD, a French CRG beamline at the ESRF. Details of the beamline operation can be found elsewhere (Proux et al., 2017). The experimental set-up is shown in Fig. 2. The electron energy was 6.0 GeV, and the ring current was 200 mA. The incident energy was selected by a cryogenically cooled double crystal Si ⟨2 2 0⟩ monochromator. Higher harmonics were suppressed by two Rh-coated mirrors, positioned at an angle of 3.9 mrad relative to the incident beam. The incident X-ray beam had a flux of approximately $9{\cdot}10^{11}$ photons s^{-1} at the sample position in a spot size of approximately 180 × 220 μm^2 (vertical × horizontal). A 5-crystal analyzer spectrometer of a Johann-type geometry (Llorens et al., 2012), equipped with Si ⟨6 6 0⟩ bent crystals with a 1 m curvature radius was used to collect the spectra in HERFD mode. The spectrometer was aligned to have the crystals in Bragg conditions at the Au $L\alpha_1$ emission line (9713 eV), corresponding to a Bragg angle of 86°. The spectra were obtained by recording the intensity of the Au $L\alpha_1$ emission line as a function of the incident energy. A combined (incident convoluted with emitted) energy resolution of 0.9 eV was determined by measuring full width at half maximum (FWHM) of the elastic peak. The photons scattered by the crystals were collected using an energy-resolved silicon-drift detector (SDD). Furthermore, the signal to background ratio was increased by selecting only the Au $L\alpha_1$ emission line in the energy window of the SDD. The As K-edge PFY spectra were measured using a second SDD and selecting the As $K\alpha$ emission lines out of

the total fluorescence yield. The incoming energy calibration was performed using the Au L_3-edge absorption energy of Au foil setting the first maximum of the first derivative to 11919 eV. Energy scans from 11,700 to 12700 eV were recorded and then averaged for each sample (the number of scans varied from 8 to 12). The samples were diluted with inert pure BN to reduce high background fluorescence from Fe. The powders were pressed into pellets, placed in a horizontal cryostat, and cooled down by liquid helium (~20 K) to improve the EXAFS data quality and prevent oxidation of As during the experiment.

The As *K*-edge absorption spectra of arsenian pyrites from the Vorontsovka deposit and model compounds ($Pb_5(AsO_4)_3Cl$, As_2O_3, $FeAs_2$, FeAsS, As_2S_3) were recorded at the STM beamline of the KSRS in transmission mode at ambient temperature. The storage-ring operating conditions were 2.3 GeV and 80–100 mA (Chernyshov et al., 2009). A Si ⟨1 1 1⟩ monochromator was used. The energy calibration was performed using the Au L_3-edge absorption energy of Au foil.

2.5. EXAFS spectra analysis

The EXAFS ($\chi_{exp}(k)$) data reduction was performed using IFEFFIT package (Ravel and Newville, 2005). After the standard procedures of pre-edge subtraction and spline background removal, average interatomic distance from the absorbing atom (R_i), coordination numbers (N_i), and Debye–Waller factors (mean square radial displacement of the atoms about R_i, σ^2) were determined via the non-linear fit of the theoretical spectra to the experimental ones with the equation

$$\chi(k) = S_0^2 \sum_{i=1}^{n} \frac{N_i F_i(k)}{R_i^2 k} e^{\frac{-2R_i}{\lambda(k)}} e^{-2\sigma_i^2 k^2} \sin(2kR_i + \varphi_i(k)). \quad (1)$$

The parameters necessary for the calculation of the theoretical spectra (photoelectron mean free path $\lambda(k)$, amplitude function $F_i(k)$, and phase shift $\varphi_i(k)$) were calculated *ab initio* using the FEFF6 program (Zabinsky et al., 1995).

3. Results

3.1. Au and As content and distribution

The products of synthesis experiments consist of fine-grained aggregates with a particle size of a few tens μm. The XRD patterns of all the samples corresponded to the pure pyrite PDF#42-1340 within the measurement error. However, SEM/EDS and XRD analyses revealed the presence of an admixture of As-S amorphous phase in Sample No. 16, arsenopyrite in Sample No. 5/2, and arsenopyrite and löllingite in sample No. 17/2 (Fig. 3a–d). The other samples contained only pure pyrite according to the SEM/EDS.

Chemical compositions of the synthesized samples are given in Table 1. The concentration of "invisible" Au varied from 75 to 360 ppm, the As content did not exceed 5 ppm (LA-ICP-MS detection limit, 2σ) in As-free samples (No. 8, 6/14, 17/1) and 1.5 wt% in arsenian pyrites (the maximum content of 6 wt% As in synthetic samples resulted from contamination with admixture of As-S amorphous phase, As sulfides and oxides). No correlation between Au and As contents was observed in synthetic samples. Despite the fact that both Au and As contents varied considerably from one sample to another and within a single grain aggregate, smooth character of LA-ICP-MS time-resolved spectra indicated the absence of micronuggets of Au-bearing phases (Fig. 4).

Chemical compositions of Au-rich fine-grained pyrite aggregates and Au-poor euhedral pyrite grains, which composed the sample of the ore from the Samolazovskoe Au-sulfide deposit, are given in Table 2. The average concentration of Au in fine-grained Au-rich arsenian pyrite, which was studied by means of XAS, is 300 ppm. In this pyrite sample the Au-As concentrations are not correlated, whereas strong positive correlations between the concentrations of Au and Ag, Tl, Te, Sb, Hg, Se, and Mn was observed (Fig. A.1).

The concentration of As in two studied pyrite samples from the Vorontsovka Carlin-type deposit is close to 1 wt%. The concentration of Au is below 10 ppm (Table 2).

3.2. XANES spectroscopy

3.2.1. Au L_3-edge

Fig. 5 shows Au L_3-edge HERFD-XANES spectra of Au-bearing pyrites together with spectra of model substances (Au and Au_2S). The spectra of Au-bearing As-free pyrite, löllingite, and arsenopyrite from Trigub et al. (2017a) are shown for comparison. The positions of the edge jump (e.j.) and the first intense feature (white line, WL) are given in Table 3. The positions of the main spectral features of As-free and arsenian pyrites are identical within the uncertainty of measurements, but differ from those of the model substances. The energy of the e.j. increases in the order Au < Au_2S < pyrite < arsenopyrite < löllingite. Accordingly, the state of Au disseminated in the matrix of pyrite differsfrom the model substances – Au and Au_2S. In addition to the e.j. position, the differences in the spectra shape of As-bearing pyrites, arsenopyrite and löllingite imply that the states of Au in these minerals are not the same.

The WL intensity, along with the e.j. position, is indicative of the oxidation state of the excited atom. The Au L_3-edge absorption is related to $2p$-$5d$ dipole-allowed transitions: $2p_{3/2} \rightarrow 5d_{5/2}/5d_{3/2}$. Therefore, the WL intensity reflects the number of empty states (holes) in the $5d_{5/2}$ and $5d_{3/2}$ orbitals above the Fermi level. Comparison of the WL intensities of the pyrite samples to those of the model substances (Au and Au_2S) implies that the "formal" oxidation state of Au in pyrite is 1+. The Au^{3+} oxidation state is ruled out due to the indicated dissimilarities in the position and intensity of the main features of Au in pyrite and $Au^{3+}Cl_4^-$ (experimental spectrum of $Au^{3+}Cl_4^-$is given in our previous studies, see, for example, Tagirov et al., 2016). The WL intensity of all pyrite samples exceeds the WL of Au_2S. Accordingly, in Au-bearing pyrites the valence electrons located on the $5d$ orbitals are shifted out of Au in comparison with Au_2S, which means that the positive charge located on "invisible" Au in pyrite is higher than the charge of Au in Au_2S. Independently of the As content and pyrite type (natural/synthetic), the samples of Au-bearing pyrites can be divided into two groups based on their WL intensity: (i) the high WL intensity group (Nos. 8522, 17/1) with WL intensity close to arsenopyrite, and (ii) the low WL intensity group – all other samples (Nos. 8, 10, 16, 6/14, 5/2, 17/2) with the WL intensity slightly above the WL of Au_2S (selected samples from both groups are shown in Fig. 5b). One of the reasons of the decrease of the WL intensity in the group (ii) samples relatively to the group (i) can be in the contamination with Au_2S. This assumption was verified by the EXAFS spectra analysis.

3.2.2. As K-edge

Fig. 6 compares As *K*-edge PFY-XANES spectra of Au-As-bearing pyrites with the references – $Pb_5(AsO_4)_3Cl$ (natural mineral, mimetite), As_2O_3 (commercial material, claudetite), As_2S_3 (natural orpiment), $FeAs_2$ (synthetic löllingite), and FeAsS (synthetic arsenopyrite). The positions of the e.j. and WL are given in Table 4. Within the references the "formal" oxidation state of As decreases in the order $Pb_5(As^{5+}O_4)_3Cl$ > $As_2^{3+}O_3$, $As_2^{3+}S_3$ > $FeAs_2^{1-}$, $FeAs^{1-}S$. Bearing in mind that the e.j., WL positions and the WL intensity are sensitive to the oxidation state of the excited atom, it is possible to estimate the oxidation state of As in arsenian pyrites by means of comparison of their spectra to the spectra of the references.

The positions of the e.j. and WL of pyrites from the Vorontsovka deposit (~11865.8 and 11867.8 eV, correspondingly) are between those of As_2S_3 and FeAsS which suggests that the most probable "formal" oxidation state of As is 1- (similarly to arsenopyrite the studied pyrite samples contain Fe, which is an electron donor; the negative charge state is consistent with the analysis of EXAFS spectra given in the next sections, whereas in Fe-free $As_2^{3+}S_3$ arsenic is considered as a cation).

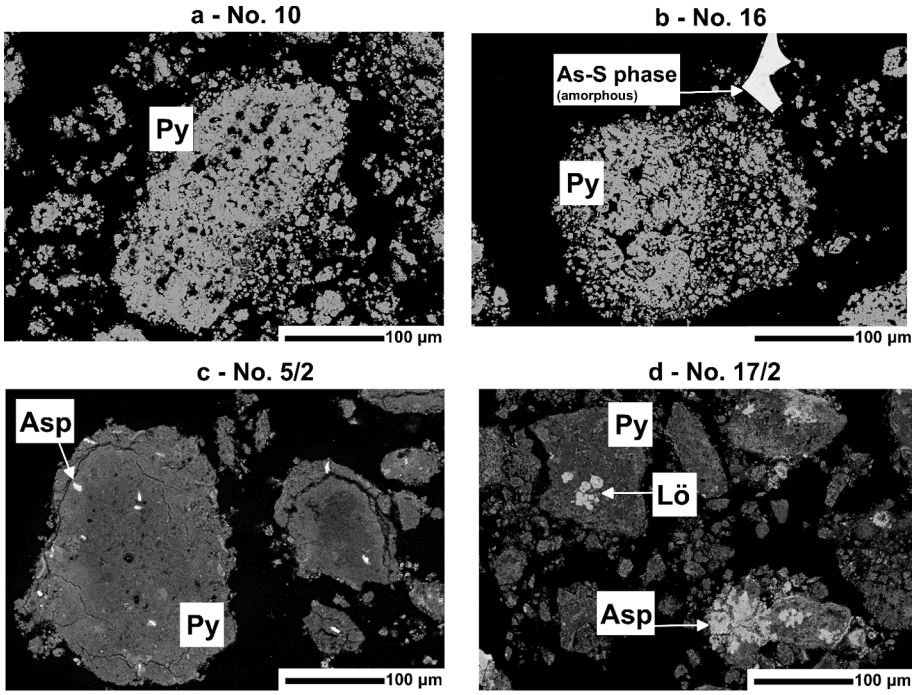

Fig. 3. Backscattered electron images of samples synthesized using hydrothermal technique. (a) – No. 10, pure pyrite (Py); (b) – No. 16, pyrite + As-S amorphous quench phase; (c) – No. 5/2, pyrite + arsenopyrite (Asp) admixture; (d) – No. 17/2, pyrite + arsenopyrite + löllingite (Lö).

In Au-bearing arsenian pyrites No. 8522 (natural, the Samolazovskoe deposit), Nos. 10, 16. and 5/2 (synthetic) the e.j. positions are identical within the uncertainty (11867.6 ± 0.5 eV). These spectra are shifted to the higher energies compared to As_2S_3, $FeAs_2$, and FeAsS (1–2.6 eV), while their e.j. positions are close to As_2O_3 (11867.7 eV). The reason for this closeness can be the presence of O in the local atomic environment of As. The WL position of these samples is between löllingite $FeAs_2^{1-}$ and As_2O_3 (Fig. 6b), but the WL intensity of

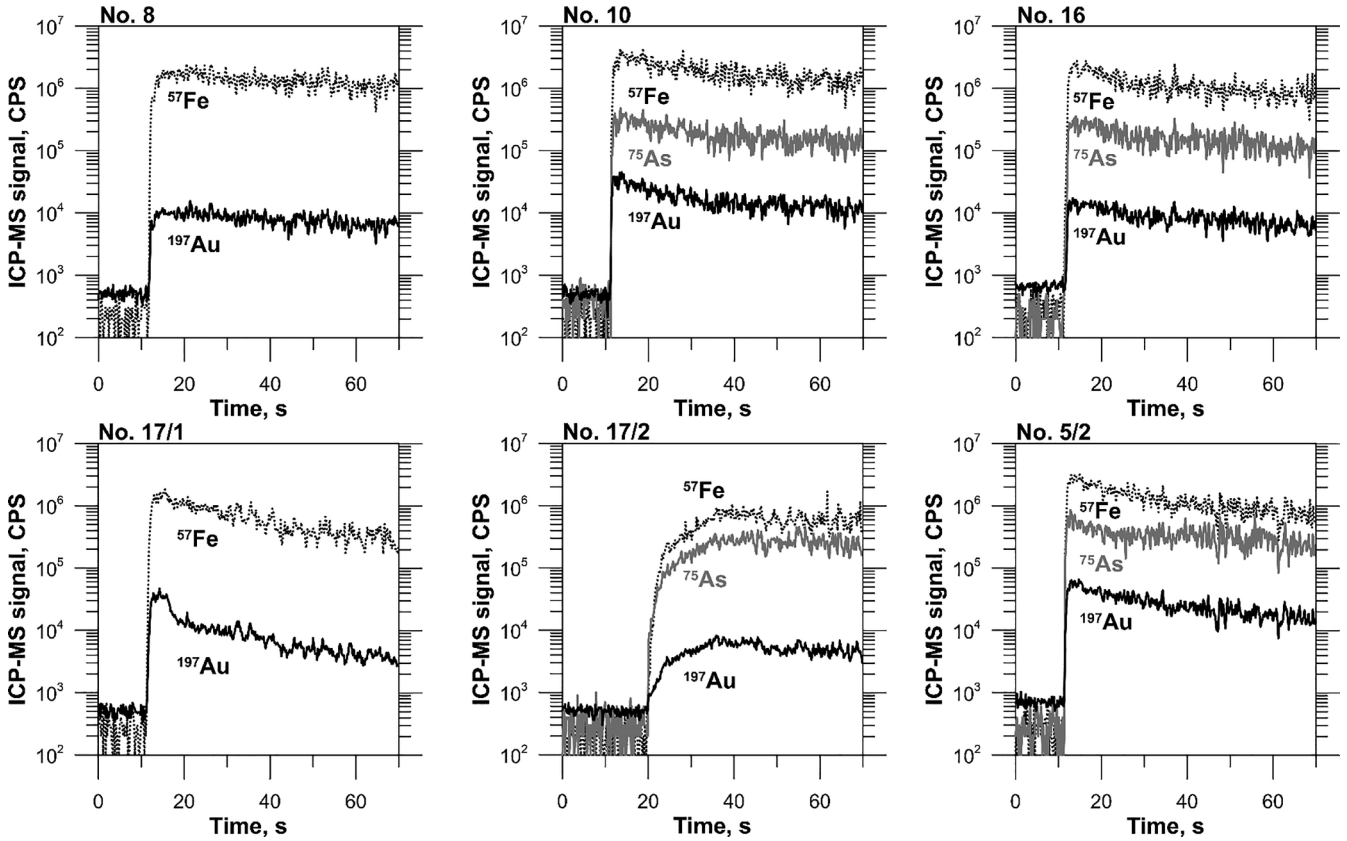

Fig. 4. Laser ablation ICP-MS time-resolved spectra of spot analyses of synthetic pyrite samples. Dotted lines – ^{57}Fe signal, black lines – ^{197}Au signal, grey lines – ^{75}As signal. Composition of samples is given in Table 1.

Table 2
Concentrations of admixtures (ppm) in natural pyrites in the ores of Samolazovskoe (Au-sulfide type) and Vorontsovka (Carlin-type) deposits.

Samolazovskoe deposit Sample No. 8522
ICP-MS analyses

Isotope	Fine-grained pyrite			Subhedral pyrite		
	Min	Max	Average (N = 22)	Min	Max	Average (N = 10)
^{51}V	192	29,620	4130	0.1	89	30
^{52}Cr	1.8	6.1	5	0.3	0.6	0.4
^{55}Mn	74.7	1390	860	0.1	168	50
^{59}Co	66.3	267	120	27.6	274	115
^{60}Ni	36.9	387	80	5.5	52	30
^{65}Cu	767	5880	1800	1.0	780	240
^{66}Zn	15.2	10,740	1370	0.8	200	50
^{71}Ga	0.3	53.7	10	0.0	0.7	0.2
^{72}Ge	1.3	8.8	5	0.9	1.2	1
^{75}As	1270	9880	3430	0.8	1730	510
^{77}Se	50	563	230	11.2	79	40
^{96}Mo	< 0.1	5.8	1.0	< 0.1	1.2	0.5
^{107}Ag	208	2760	990	< 0.1	355	115
^{111}Cd	0.7	35.6	7	< 0.1	2.1	1.0
^{115}In	< 0.1	0.8	0.2	< 0.1	< 0.1	< 0.1
^{118}Sn	0.7	46.7	10	0.3	3.0	1
^{121}Sb	1090	10,580	5580	0.1	2260	710
^{125}Te	11.5	571	150	< 0.1	36	10
^{182}W	0.1	251	50	< 0.1	182	30
^{197}Au	21.6	656	300	0.3	73	30
^{201}Hg	45.6	523	210	0.4	67	20
^{205}Tl	262	3560	1800	< 0.1	578	190
^{208}Pb	1140	31,400	5900	1.1	2620	810
^{209}Bi	5.8	11,500	600	0.3	28	10
LA-ICP-MS analyses, average, ppm ± 2σ						
^{75}As	3400 ± 30			not analyzed		
^{197}Au	300 ± 30			not analyzed		
Vorontsovka deposit Sample No. Vr-134-7 LA-ICP-MS analyses, average, ppm ± 2σ						
^{75}As	9000 ± 130					
^{197}Au	9 ± 1					
Vorontsovka deposit Sample No. Vr-134–13 LA-ICP-MS analyses, average, ppm ± 2σ						
^{75}As	14300 ± 200					
^{197}Au	8 ± 1					

Table 3
Positions of edge jump (e.j.) and the first intense feature (white line, WL) of Au L_3-edge spectra recorded for reference materials and Au-(As)-pyrites (± 0.5 eV).

Au L_3-edge XANES

Sample/reference ID	Feature	Position, eV
Reference materials		
Au	e.j.	11919.0
	WL	11922.0
Au_2S	e.j.	11919.8
	WL	11922.4
Löllingite[1]	e.j.	11921.0
$FeAs_2$	WL	11922.9
Arsenopyrite[1]	e.j.	11920.6
FeAsS	WL	11922.4
Hydrothermal pyrite[1]	e.j.	11919.5
FeS_2	WL	11921.2
Natural pyrites		
No. 8522, natural As-pyrite	e.j.	11920.7
FeS_2	WL	11922.0
Products of high temperature synthesis		
No. 8, synthetic As- free pyrite	e.j.	11920.2
FeS_2	WL	11921.6
No. 10, synthetic arsenian pyrite	e.j.	11920.3
FeS_2	WL	11921.8
No. 16, synthetic arsenian pyrite	e.j.	11920.3
FeS_2	WL	11922.0
No. 6/14, synthetic As- free pyrite	e.j.	11920.2
FeS_2	WL	11921.6
Products of low temperature synthesis		
No. 17/1, synthetic As-free pyrite	e.j.	11920.3
FeS_2	WL	11921.8
No. 17/2, synthetic arsenian pyrite	e.j.	11920.5
FeS_2 + FeAsS + $FeAs_2$	WL	11921.7
No. 5/2, synthetic arsenian pyrite	e.j.	11920.3
FeS_2	WL	11921.8

[1]adopted from Trigub et al. (2017a).

As-bearing pyrites is much greater than that of $FeAs^{1-}S$, $FeAs_2^{1-}$, and $As_2^{3+}S_3$. This confirms the presence of O in the local atomic environment of As. Due to the greater electronegativity of O compared to S the average electron density of the 4*p* electronic shell of As in arsenian pyrites is lower than the electron density of S-bearing model substances. This fact explains the high WL intensity in O-bearing samples as it is proportional to the probability of the $1s \rightarrow 4p_{3/2}/4d_{1/2}$ dipole-allowed transitions. Thus, we suggest that in these samples of As-bearing pyrites both O and S can present in the local atomic environment of As.

In sample No. 5/2 the second feature at 11874.5 eV is attributed to

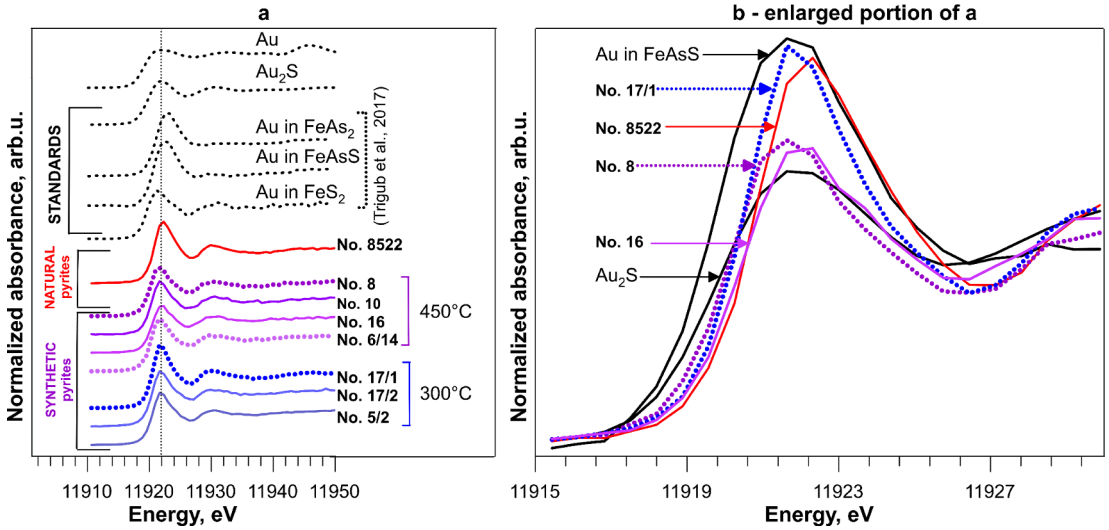

Fig. 5. Au L_3-edge HERFD-XANES spectra of Au-bearing pyrites and model substances. (a) – full XANES region; (b) – white line region. All the Au L_3-edge spectra recorded in the present study correspond to cryogenic temperature, data of Trigub et al. (2017a) were obtained at ambient temperature.

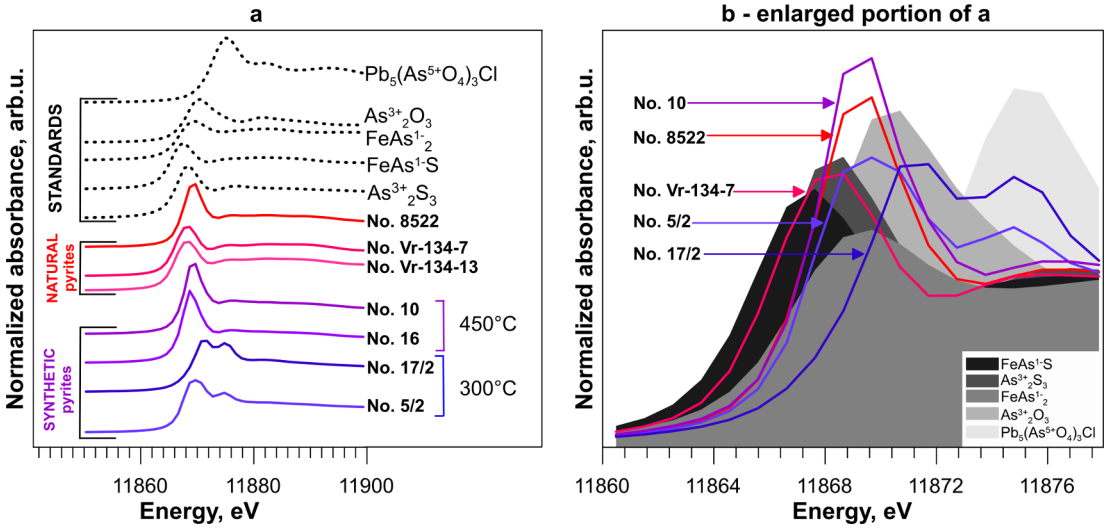

Fig. 6. As *K*-edge PFY-XANES spectra of arsenian pyrites and model substances. (a) – full XANES region, (b) – white line region. The shaded area shows the spectra of the model substances. The spectra of pyrites from Vorontsovka deposit (VR-134-7, VR-134-13) and the spectra of standards were recorded at ambient temperature, the spectra of all other samples were recorded at cryogenic temperature.

Table 4
Positions of edge jump (e.j.) and the first intense feature (white line, WL) of As *K*-edge spectra recorded for reference materials and arsenian pyrites (± 0.5 eV).

As *K*-edge XANES		
Sample/Reference ID	Feature	Position, eV
Reference materials		
Mimetite	e.j.	11872.3
$Pb_5(AsO_4)_3Cl$	WL	11874.8
Claudetite[1]	e.j.	11867.7
As_2O_3	WL	11870.0
Löllingite	e.j.	11866.3
$FeAs_2$	WL	11869.4
Arsenopyrite	e.j.	11865.3
FeAsS	WL	11867.1
Orpiment	e.j.	11866.4
As_2S_3	WL	11868.3
Natural arsenian pyrites		
No. 8522	e.j.	11867.6
FeS_2	WL	11869.3
No. Vr-134–7	e.j.	11865.9
FeS_2	WL	11867.8
No. Vr-134–13	e.j.	11865.8
FeS_2	WL	11867.8
Products of high temperature synthesis		
No. 10	e.j.	11867.9
FeS_2	WL	11869.2
No. 16	e.j.	11867.4
FeS_2	WL	11868.7
Products of low temperature synthesis		
No. 17/2	e.j.	11869.6
FeS_2 + FeAsS	WL	11871.3
	B	11874.9
No. 5/2	e.j.	11867.5
FeS_2 + FeAsS	WL	11869.7
	B	11874.6

[1]adopted from Newville et al. (1999).

the presence of As^{5+}. Therefore, in this sample, in addition to As^{1-}, As presents in both 3+ and 5+ "formal" oxidation states and is expected to have O and S neighboring atoms. In sample No. 17/2 the second feature (11875 eV) is more intense than in sample No. 5/2 suggesting a higher As^{5+} concentration.

Thus, the analysis given above suggests that the oxidation state of As in the studied arsenian pyrites varies from 1 − (arsenian pyrites from the Vorontsovka deposit) to 3+/5+ (low-temperature synthetic arsenian pyrites No. 5/2 and 17/2). The shape of the spectra and positions of the spectral features imply that S predominates in the local atomic environment of As in the samples from the Vorontsovka deposit, whereas both S and O present in the sample from the Samolazovskoe deposit and in the samples of synthetic pyrites.

3.3. EXAFS spectra fitting

The EXAFS spectra of Au L_3-edge and As *K*-edge are shown in Fig. 7 a-h and 8 a-f, correspondingly. Results of the EXAFS spectra fitting are given in Fig. 7 i, Tables 5 and 6 (Au L_3-edge), and Table 7 (As *K*-edge).

3.3.1. Au L_3-edge

The best fit of the experimental spectrum of natural arsenian pyrite Sample No. 8255 was achieved when Au substitutes for Fe in the pyrite structure (N_S = 5.5 ± 0.8, $R_{Au\text{-}S}$ = 2.40 ± 0.01 Å). Attempts to introduce the heavy As atom to the 1st coordination shell of Au resulted in its elimination, which means that As is absent in the vicinity of Au. A slight decrease of the 1st coordination number relatively to the pure pyrite structure (N_S = 6) probably stems from the presence of a small admixture of Au_2S-like clusters/inclusions. Data of Table 5 indicate that $R_{Au\text{-}S}$ and $R_{Au\text{-}Fe}$ in the distant coordination shells are close to pure FeS_2 (within the uncertainty of the calculated values). The presence of the heavy Fe atom in the 2nd shell is confirmed by the backward Fourier transform of the EXAFS spectra: its maximum is located at high value of the photoelectron wavenumber *k* which is not characteristic of the light S atom (Fig. A.2a). Similarly to the 1st shell, the As atoms are absent in the distant (2nd and 3rd) coordination shells of Au which correspond to the pyrite crystal structure. It is worth to note that the spectrum of natural arsenian pyrite No. 8522, as well as the Fourier transform (FT) of the spectrum, are very similar to those of As-free synthetic pyrite No. 17/1. The EXAFS spectra fits of these two samples also resulted in similar parameters of the local atomic environment of Au. This means that despite the presence of 0.3 wt% As in the sample of natural arsenian pyrite, its effect on the parameters of the local atomic environment of Au is negligible.

In synthetic As-free and arsenian pyrites No. 8, 10, 16, 6/14 obtained at 450 °C, and 5/2 obtained at 300 °C Au atom is also surrounded only by S atoms. The $R_{Au\text{-}S}$ in these samples varies from 2.32 to 2.45 Å.

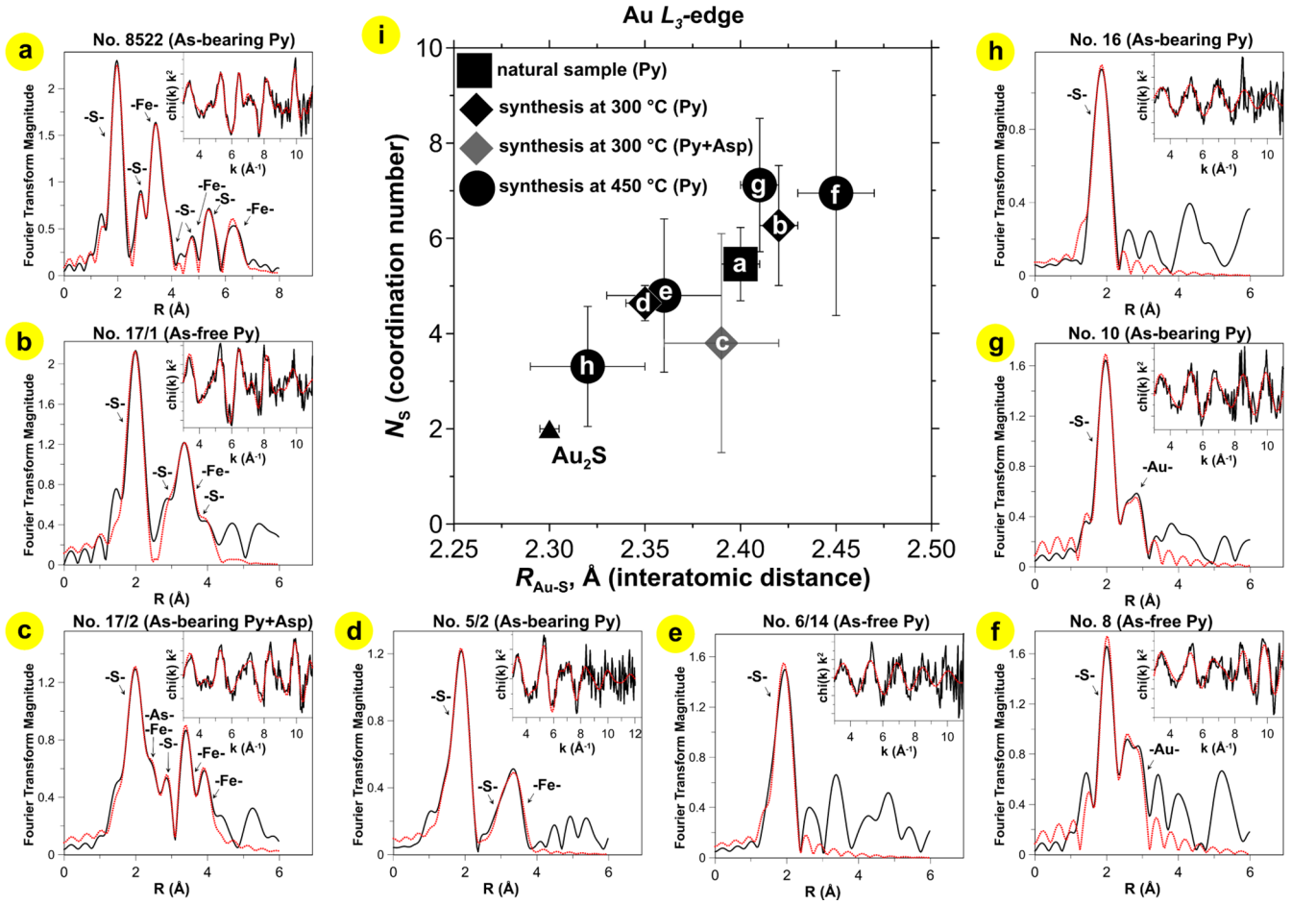

Fig. 7. The k^2-weighted background-subtracted Au L_3-edge EXAFS spectra and their Fourier transforms (FT, not corrected for phase shift). (a) natural pyrite sample; (b-h) synthetic pyrites, parameters of synthesis 300 °C/P_{sat} (b–d) and 450 °C/1 kbar (e–h). Solid black lines – experiment, dotted red lines – fit results. Scattering atoms are indicated near FT peaks. Fit results are listed in Table 5. (i)- interatomic distance (R_{Au-S}) as a function of coordination number (N_S). Pyrites contain both Au in solid solution and Au_2S-like clusters. The presence Au_2S-like clusters resulted in decrease of the R_{Au-S} and N_S in the 1st coordination sphere. All the spectra were recorded at cryogenic temperature. (For interpretation of the references to colour in this figure legend, the reader is referred to the web version of this article.)

This difference exceeds the uncertainty of the calculated Au-S distances. The calculated values of N_S also vary significantly – from 3 to 7, but with high uncertainty of the single values. These samples can be divided into three groups according to the composition of the distant coordination shells of Au: (i) the distant coordination shells are disordered – no distant-coordination-shell atoms can be identified (Samples No. 16, 6/14), (ii) the Au atoms are present in the 2nd shell (Nos. 8 and 10), and (iii) the Fe and S atoms are present in the distant coordination shells (No. 5/2).

In the group (i) samples the Au-S distance in the 1st shell falls between the distance of the solid solution Au (2.40–2.42 Å in Samples No. 8522 and 17/1) and that of Au_2S (2.30 Å, c.f., Filimonova et al., 2019). Therefore, we suppose that these samples contain both forms of Au with the notable contribution of Au_2S-like inclusions or clusters. Note that no Au_2S phase was detected by means of the SEM/EDS analysis and, therefore, this form of Au also can be considered as "invisible". In the group (ii) samples there are Au atoms in the 2nd coordination shell of the excited Au atom. The presence of the distant-coordination-sphere Au atoms can result from either admixture of Au_2S or clustering of the solid solution Au. The distance between Au and the nearest S neighbors exceeds notably the Au-S distance in Au_2S but is close to the solid solution Au, whereas the N_S is close to 6 which is characteristic of the pyrite structure but differs from $N_S = 2$ in Au_2S. Therefore, we suppose that in these samples the formation of clusters of the solid solution Au takes place. In Sample No. 5/2 (type iii) the atoms of S and Fe were detected in the 2nd and 3rd coordination shells, respectively, at the distances close to those of pure pyrite. However, in the 1st coordination shell, the N_S and R_{Au-S} values are smaller than the values of the solid solution Au. This implies that in this sample, similarly to the group (i) samples, both solid solution Au and Au_2S coexist. The content of arsenopyrite, which was found in Sample No. 5/2 by means of the SEM/EDS analysis, is insufficient to be detected by means of XAS.

The EXAFS spectrum of Sample No. 17/2, which was synthesized at 300 °C, results from a combination of signals from several Au-bearing phases. We identified these phases as As-bearing pyrite, arsenopyrite or löllingite, and Au_2S-like clusters. Table 6 compares the results of the EXAFS spectra fitting of Sample No. 17/2 with the data on the Au local atomic environments pertinent to the phases which are supposed to compose the sample. The presence of the admixture of Au_2S-like clusters results in the decrease of the N_S and R_{Au-S} in the 1st shell from 6 to 3.8 and from 2.41 to 2.39 Å, respectively. The presence of Au incorporated into the crystal structure of As-bearing phases (arsenopyrite and/or löllingite) can be identified in the Sample No. 17/2 due to the following reasons:

(i) a heavy atom (As) presents at a distance of ca. 2.54 Å which is close to the Au-As distance in arsenopyrite ($N_{As} = 3$, $R_{Au-As} \sim 2.53$ Å) and löllingite ($N_{As} = 6$, $R_{Au-As} \sim 2.52$ Å, Trigub et al., 2017a);
(ii) the distant coordination shells of Au are best described by the combination of pure pyrite and arsenopyrite/löllingite structures. The presence of Fe atoms at the distances of 2.9 Å and 4.1 Å is characteristic of the arsenopyrite and löllingite structures, there are

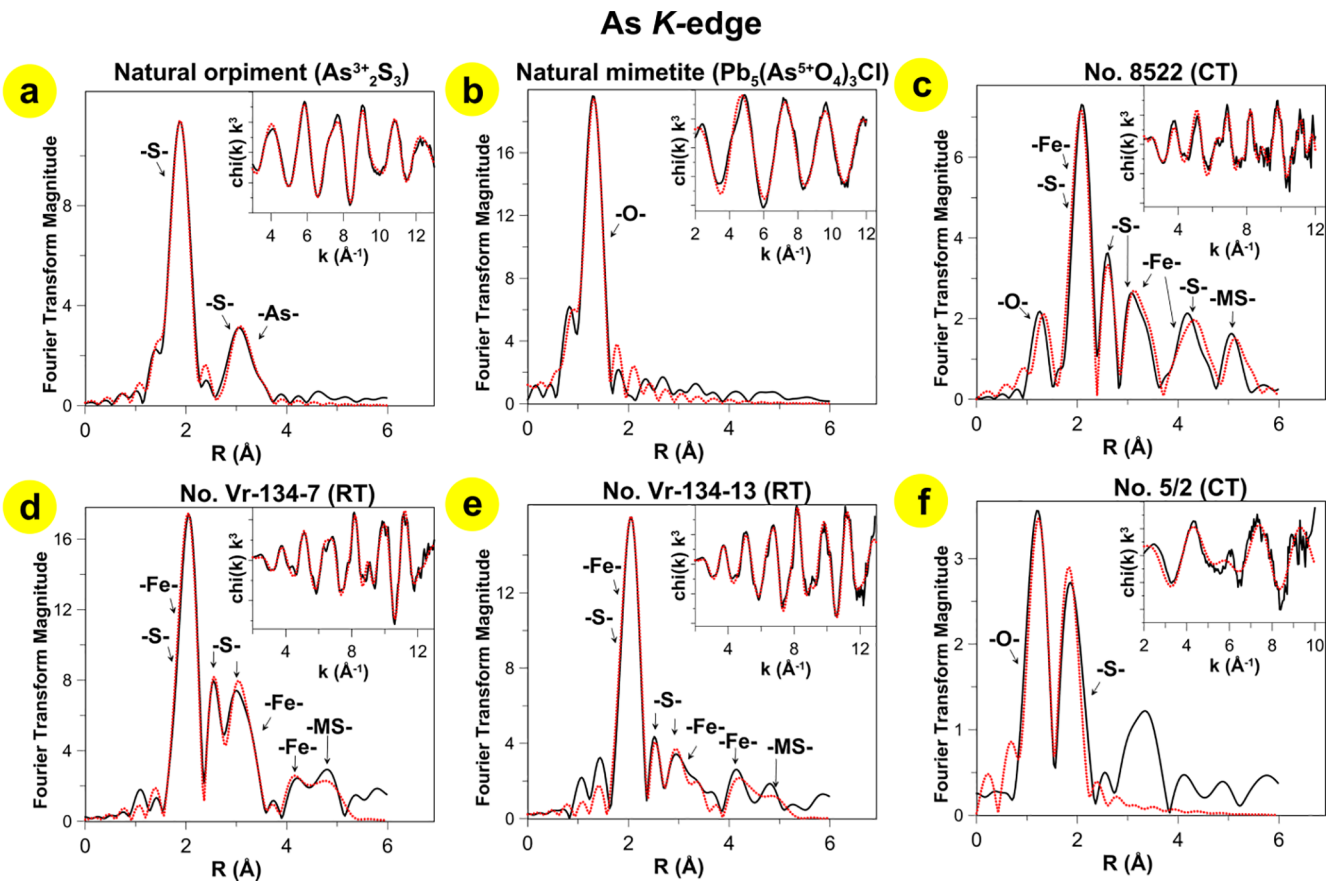

Fig. 8. The k^3-weighted background-subtracted As *K*-edge EXAFS spectra and their Fourier transforms (FT, not corrected for phase shift). (a, b) – model substances. (c–e) – natural samples. (f) – pyrite synthesized at 300 °C/P_{sat}. Solid black lines – experiment, dotted red lines – fit results. Scattering atoms are indicated near FT peaks. Fit results are listed in Table 7. CT – cryogenic temperature, RT – ambient temperature. (For interpretation of the references to colour in this figure legend, the reader is referred to the web version of this article.)

no Fe atoms at this distance in the structure of pyrite (last column of Table 5). In the structure of Au-bearing löllingite, the Au-Fe distance of 4.23 Å (Trigub et al., 2017a; Table 6, this study) is somewhat larger than the distance of 4.12 Å determined in the Sample No. 17/2. In the structure of pure arsenopyrite the Fe atoms are located at 3.94 – 4.10 Å (this distance was not reported for the Au-bearing arsenopyrite in Trigub et al., 2017a, but usually the distances in the distant coordination shells of metal in pure and Au-bearing sulfides are similar). The similar positions of the distant-coordination-shell Fe atoms in Sample No. 17/2, arsenopyrite and löllingite do not allow to discriminate between arsenopyrite and löllingite, but only indicate that one of these minerals or both present in this sample.

Regardless of the pyrite type and composition (natural or synthetic, pure or arsenian) the interatomic distances $R_{Au\text{-}S}$ are correlated with the number of the nearest S atoms N_S (Fig. 4 *i*). The observed dependence can be accounted for by the presence of two dominant forms of Au. The first form is the solid solution Au. Incorporation of Au into the cationic position of the pyrite crystal structure (N_S = 6) results in the increase of $R_{Au\text{-}S}$ by 0.15 Å up to 2.41 Å in comparison with $R_{Fe\text{-}S}$ = 2.26 Å in the structure of pure pyrite. The second form we identify as Au_2S-like clusters/inclusions. Due to low values of coordination number and interatomic distances in the 1st shell of Au in Au_2S (N_S = 2 and $R_{Au\text{-}S}$ = 2.30 Å, c.f., Filimonova et al., 2019) admixture of Au_2S-like clusters causes significant decrease of the measured $R_{Au\text{-}S}$ and N_S which was observed in the studied series of samples. Because of the presence of the two forms of Au the uncertainties of calculated values of interatomic distances and coordination numbers are quite large.

3.3.2. As K-edge

According to the XANES spectra analysis, the oxidation state of As in the samples of natural arsenian pyrites from the Vorontsovka deposit (Nos. Vr-134-7 and Vr-134-13) is close to 1-. These results are confirmed by the EXAFS spectra fits. In these samples, the EXAFS spectra are best described by the model of the solid solution with S substituted by As in pyrite crystal structure. Due to a larger As atomic radius the As-S and As-Fe interatomic distances increase slightly, by 0.1 and 0.06–0.08 Å, respectively, relatively to the pure pyrite structure. In sample No. 8522 (the Samolazovskoe deposit) O atoms are the nearest neighbors of As due to the presence of As^{3+} oxide.

In all the studied samples (with an ecxeption of the Sample No. 17/2, see below) no As atoms were observed around the excited As atom. Incorporation of As atoms to the 1st coordination shell of As resulted in their elimination during the experimental spectra fits. Savage et al. (2000) found that the best fit of the As *K*-edge spectra of natural arsenian pyrite is attained when the 2nd coordination shell comprises 4 S atoms at a distance of 3.10 Å and 3 As atoms at a distance of 3.17 Å. Implementation of the Savage et al. (2000) model resulted in the significant increase of the As-S and As-As distances: both types of atoms moved to a distance of 3.23 Å. The equivalence of the distances looks unrealistic because of the significant difference in the ionic radii of As and S. Moreover, the goodness of the fit decreased significantly in comparison with the As-free model (reduced χ^2 increased from 18 to 83). Therefore, we suggest the absence of As-As clustering.

The spectrum of synthetic pyrite Sample No. 5/2 is described by a combination of spectra of As oxides and the solid solution As in pyrite. The nearest to As atoms O and S are located at the distances of1.72 and 2.26 Å, correspondingly which is close to the values determined in the

Table 5
Gold local atomic structure determined by EXAFS spectra fits (the fits are performed in *R*-space unless otherwise indicated, k^2-weighting). Uncertainties are calculated by ARTEMIS program. Numbers without uncertainties were fixed during the fit.

Atom	Experimental data[1]					Theoretical data[2]
	N	*R*, Å	σ^2, Å^2	ΔE^0, eV	Red. χ^2 (R-factor)	*R*, Å *(N)*
Au L_3-edge[3]						
Natural pyrite						
No. 8522: *R*-range: 1.3 – 6.6, *k*-range: 3 – 11						Au_2S and FeS_2[a,b]
S	5.5 ± 0.8	2.40 ± 0.01	0.002 ± 0.001	6.7 ± 1.2	1 (0.018)	*2.30 (2)*/2.26 (6)
S	8	3.45 ± 0.02	0.007 ± 0.002			3.45 (6) and 3.60 (2)
Fe	12	3.83 ± 0.01	0.003 ± 0.001			3.83 (12)
S	6	4.35 ± 0.07	0.013 ± 0.012			4.45 (6)
S	18	5.32 ± 0.08	0.017 ± 0.016			5.16 and 5.26 (6 and 12)
Fe	6	5.43 ± 0.05	0.003 ± 0.005			5.42(6)
S	26	5.88 ± 0.02	0.003 ± 0.002			5.78, 5.87 and 6.43 (2, 12, 12)
Fe	24	6.68 ± 0.02	0.003 ± 0.002			6.64 (24)
High temperature synthesis (450 °C/1 kbar)						
No. 8: *R*-range: 1.3 – 3.1, *k*-range: 3 – 11						Au_2S and FeS_2[a,b]
S	7.0 ± 2.6	2.45 ± 0.02	0.005 ± 0.005	13.8 ± 2.5	3 (0.018)	*2.30 (2)*/2.26 (6)
Au	9.1 ± 2.3	2.62 ± 0.01	0.005 ± 0.002			*3.68 (12)*/–
No. 10: *R*-range: 1.3 – 3.1, *k*-range: 3 – 11						Au_2S and FeS_2[a,b]
S	7.1 ± 1.4	2.41 ± 0.01	0.005 ± 0.001	11.5 ± 1.4	0.5 (0.006)	*2.30 (2)*/2.26 (6)
Au	12.6 ± 5.4	2.59 ± 0.01	0.011 ± 0.003			*3.68 (12)*/–
No. 16: *R*-range: 1.3 – 2.3, *k*-range: 3 – 11						Au_2S and FeS_2[a,b]
S	3.3 ± 1.3	2.32 ± 0.03	0.004 ± 0.004	1.7 ± 4.7	3 (0.023)	*2.30 (2)*/2.26 (6)
No. 6/14: *R*-range: 1.3 – 2.3, *k*-range: 3 – 11						Au_2S and FeS_2[a,b]
S	4.8 ± 1.6	2.36 ± 0.03	0.005 ± 0.004	6.2 ± 3.9	1 (0.015)	*2.30 (2)*/2.26 (6)

Atom	Experimental data[1]					Theoretical data[2]	
	N	*R*, Å	σ^2, Å^2	ΔE^0, eV	Red. χ^2 (R-factor)	*R*, Å (*N*)	
Low temperature synthesis (300 °C/Psat)							
No. 17/1: *R*-range: 1.3–4.3, *k*-range: 3–11						Au_2S and FeS_2[a,b]	
S	6.3 ± 1.3	2.42 ± 0.01	0.005 ± 0.002	3.2 ± 1.7	3 (0.029)	*2.30 (2)*/2.26 (6)	
S	8	3.49 ± 0.04	0.010 ± 0.005			3.45 (6) and 3.60 (2)	
Fe	12	3.84 ± 0.02	0.009 ± 0.002			3.83 (12)	
S	6	4.38 ± 0.05	0.006 ± 0.07			4.45 (6)	
No. 17/2: *R*-range: 1.3–4.3, *k*-range: 3–11						Au_2S and FeS_2[a,b]	FeAsS (< 5%)[c]
S	3.8 ± 2.3	2.39 ± 0.03	0.008 ± 0.009	7.2 ± 2.1	2 (0.005)	*2.30 (2)*/2.26 (6)	2.23 (3)
As	2.2	2.54 ± 0.04	0.005 ± 0.012			–	2.37–2.41 (3)
Fe	1	2.91 ± 0.04	0.001 ± 0.007			–	2.73 (1)
S	8	3.43 ± 0.05	0.018 ± 0.007			3.45 (6) and 3.60 (2)	–
Fe	12	3.88 ± 0.02	0.008 ± 0.002			3.83 (12)	–
Fe	6	4.12 ± 0.02	0.001 ± 0.001			–	3.94–4.10 (6)
No. 5/2: *R*-range: 1.3 – 3.7, *k*-range: 3 – 12						Au_2S and FeS_2[a,b]	
S	4.6 ± 0.4	2.35 ± 0.01	0.007 ± 0.001	2.2 ± 1.0	0.2 (0.005)	*2.30 (2)*/2.26 (6)	
S	1.9 ± 1.4	3.42 ± 0.03	0.008 ± 0.008			3.45 (6) and 3.60 (2)	
Fe	12	3.81 ± 0.01	0.015 ± 0.001			3.83 (12)	

[1] *N* – coordination number, *R* – interatomic distance between the absorbing and neighboring atoms (Å), σ^2 – Debye-Waller factor (Å^2); *R*-factor (the fraction of misfit between experiment and model) and Red. χ^2 (reduced chi-square – parameter including the degree of freedom and uncertainties of each data point) – goodness-of-fit statistics; [2]data from: [a]Filimonova et al. (2019), [b]Brostigen and Kjekshus (1969), [c]Bindi et al. (2012); [3]amplitude reduction factor S_0^2 = 0.84 adopted from Filimonova et al. (2019).

Table 6
Comparison of Au local atomic environment in Sample No. 17/2 and Au-bearing phases which were detected in this sample.

Sample No. 17/2[1]			Au_2S[2]			*Solid solution Au*								
						Au in pyrite[3]			Au in arsenopyrite[4]			Au in löllingite[4]		
Atom	N[5]	*R*, Å[5]	Atom	*N*	*R*, Å	Atom	*N*	*R*, Å	Atom	*N*	*R*, Å	Atom	*N*	*R*, Å
S	3.8	2.39	S	2	2.30	S	6	2.41	S	3	2.47	As	6	2.52
As	2.2	2.54	Au	12	3.68	S	8	3.47	As	3	2.53	Fe	2	3.00
Fe	1	2.91				Fe	12	3.83	Fe	1	2.98	As	4	3.88
S	8	3.43				S	6	4.37	Fe	1	3.66	As	6	4.06
Fe	12	3.88							S	4	3.72–3.78	Fe	8	4.23
Fe	6	4.12							As	4	3.79–3.92			
									Fe[6]	6	3.94–4.10			

Experimental data from [1] this study, [2] Filimonova et al. (2019), [3] this study, Samples No. 17/1 and 8522, average, [4] Trigub et al. (2017a); [5]*N* – coordination number, *R* – interatomic distance between the absorbing and neighboring atoms (Å); [6] adopted from the pure arsenopyrite structure;

Table 7
Arsenic local atomic environment in pyrite determined by EXAFS spectra fits (the fits are performed in *R*-space unless otherwise indicated, k^3-weighting). Uncertainties are calculated by ARTEMIS program. Numbers without uncertainties were fixed during the fit.

Atom	Experimental data[1]					Theoretical data[2]
	N	*R*, Å	σ^2, Å^2	$\triangle E^0$, eV	Red. χ^2 (R-factor)	*R*, Å (*N*)
As *K*-edge[3]						
Reference materials						
Natural mimetite: *R*-range: 1.1–2.0, *k*-range: 3–13						$Pb_5(As^{5+}O_4)_3Cl$[a]
O	4	1.70 ± 0.01	0.002 ± 0.002	7.9 ± 3.0	1320 (0.012)	1.66-1.75 (4)
Natural orpiment: *R*-range: 1.1–3.5, *k*-range: 3–13						$As_2^{3+}S_3$[b]
S	3	2.28 ± 0.01	0.004 ± 0.001	7 ± 1.0	175 (0.012)	2.27-2.28 (3)
S	1	3.38 ± 0.04	0.003 ± 0.003			3.40 (1)
As	2	3.54 ± 0.03	0.008 ± 0.003			3.49-3.50 (2)
Natural pyrites						
No. 8522: *R*-range: 1.1–5.4, *k*-range: 2–12						$\underline{FeAs^{5+}O_4{\cdot}2H_2O/As_2^{3+}O_3}$, Fe(S, $As^{1-})_2$[c,d,e]
O	0.4 ± 0.5	1.74 ± 0.05	0.002 ± 0.010	8.6 ± 1.8	18 (0.066)	$\underline{1.70\text{-}1.80\ (4)}$
S	1	2.25 ± 0.04	0.002 ± 0.002			2.18 (1)
Fe	3	2.32 ± 0.02	0.008 ± 0.002			2.26 (3)
S	6	3.18 ± 0.02	0.012 ± 0.003[5]			3.07 (6)
S	6	3.45 ± 0.05	0.012 ± 0.003[5]			3.32 (6)
Fe	4	3.56 ± 0.02	0.008 ± 0.003			3.45 (3) and 3.60 (1)
Fe	3	4.24 ± 0.08	0.015 ± 0.010			4.45 (3)
S	3	4.74 ± 0.03	0.002 ± 0.002			4.53 (3)
MS[4]	3	5.58 ± 0.04	0.004 ± 0.004			5.34 (3)
No. Vr-134-7: *R*-range: 1.1–5.1, *k*-range: 2–13						Fe(S, $As^{1-})_2$[e]
S	1	2.25 ± 0.04	0.002 ± 0.004	7.6 ± 0.9	49 (0.014)	2.18 (1)
Fe	3	2.33 ± 0.01	0.003 ± 0.001			2.26 (3)
S	6	3.07 ± 0.01	0.005 ± 0.001[5]			3.07 (6)
S	6	3.33 ± 0.01	0.005 ± 0.001[5]			3.32 (6)
Fe	4	3.49 ± 0.01	0.007 ± 0.002			3.45 (3) and 3.60 (1)
Fe	3	4.62 ± 0.02	0.004 ± 0.002			4.45 (3)
MS[6]	6	5.25 ± 0.02	0.007 ± 0.002			5.30
No. Vr-134-13: *R*-range: 1.1–5.2, *k*-range: 2–13						Fe(S, $As^{1-})_2$[e]
S	1	2.28 ± 0.03	0.002 ± 0.003	8.2 ± 1.6	60 (0.025)	2.18 (1)
Fe	3	2.34 ± 0.01	0.003 ± 0.001			2.26 (3)
S	6	3.11 ± 0.03	0.013 ± 0.003			3.07 (6)
S	6	3.35 ± 0.02	0.005 ± 0.002			3.32 (6)
Fe	4	3.43 ± 0.04	0.011 ± 0.006			3.45 (3) and 3.60 (1)
Fe	3	4.61 ± 0.03	0.006 ± 0.002			4.45 (3)
MS[6]	6	5.27 ± 0.06	0.011 ± 0.005			5.30
Low temperature synthesis (300 °C/Psat)						
No. 5/2: *R*-range: 0.9–2.9, *k*-range: 2–10						$\underline{FeAs^{5+}O_4{\cdot}2H_2O/As_2^{3+}O_3}$, Fe(S, $As^{1-})_2$[c,d,e]
O	1.1 ± 0.6	1.72 ± 0.02	0.003 ± 0.005	6.8 ± 4.4	23 (0.073)	$\underline{1.70\text{-}1.80\ (4)}$
S	1	2.26 ± 0.03	0.006 ± 0.003			2.18 (1)

[1] *N* – coordination number, *R* – interatomic distance between the absorbing and neighboring atoms (Å), σ^2 – Debye-Waller factor (Å^2); *R*-factor (the fraction of misfit between experiment and model) and Red. χ^2 (reduced chi-square – parameter including the degree of freedom and uncertainties of each data point) – goodness-of-fit statistics;
[2] calculated using crystallographic data from [a]Dai et al. (1991), [b]Kampf et al. (2011), [c]Kitahama et al. (1975), [d]Pertlik (1978), [e]Brostigen and Kjekshus (1969);
[3] amplitude reduction factor $S_0^2 = 0.90$ calculated by fitting the spectra of mimetite and orpiment;
[4] MS – multiple scattering, corresponds to As0-S-Fe-S-As0 path;
[5] Parameters are fixed to be equal;
[6] MS corresponds to As0- Fe-S-As0 path.

samples of natural arsenian pyrite No. 8522. Our attempts to fit the EXAFS spectra of all other synthetic arsenian pyrites failed to produce a set of consistent data because these samples represent a mixture of several As-bearing phases: according to XANES spectra analysis (Section 3.2.2), the spectra result from the superimposing of the signals from the As^{1-} solid solution, As sulfide (or sulfides), and As^{3+} and As^{5+} oxides.

The spectrum of Sample No. 17/2 cannot be adequately presented as a linear combination of the listed above phases. Examination of the backward Fourier transform of the spectrum of this sample showed that, in contrast to the other samples, Au presents in the distant coordination shell of As at a distance of 2.5–2.6 Å (Fig. A.2b). The latter distance is similar to the Au-As distance calculated from Au L_3-edge EXAFS spectra fit (N_{As} = 2.2, $R_{Au\text{-}As}$ = 2.54 ± 0.04 Å, Table 5). The presence of Au atom at this distance confirms that Sample No. 17/2, in addition to the solid solution Au in the pyrite matrix, contains Au-bearing arsenopyrite or löllingite.

4. Discussion

The results of our study demonstrate that in the ores of hydrothermal deposits "invisible" Au in the matrix of pyrite exists in the form of the solid solution Au and Au_2S-like particles or clusters. These two forms coexist, their concentration ratio is governed by kinetic factors rather than physicochemical parameters of the ore-forming process. In the solid solution state the Au^{1+} substitutes for Fe. Due to the large ionic radius of Au the distance between the metal and the nearest six S atoms increases from $R_{Fe\text{-}S}$ = 2.26 Å (pure pyrite) to $R_{Au\text{-}S}$ = 2.41 Å (Au-bearing pyrite). Distortions of the atomic structures are localized around Au atoms and are eliminated at $R > 3$ Å. The presence of

substantial amount of Au_2S-like clusters (pure Au_2S: N_S = 2 and R_{Au-S} = 2.30 Å) results in the significant decrease of the calculated coordination number and interatomic distance Au-S in the 1st coordination shell. The presence of As does not affect the local atomic environment of the solid solution Au: no As was detected by means of the Au L_3-edge EXAFS spectra treatment, and no Au was observed around As by the As *K*-edge EXAFS spectra fits. Moreover, the examination of Au L_3-edge EXAFS spectra of As-free and arsenian pyrites revealed similar atomic configurations around Au. Therefore, both Au and As are statistically (randomly) distributed in the matrix of pyrite without the Au-As clustering. These results are consistent with data of Merkulova et al. (2019) who also determined the state of Au in a sample of natural arsenian pyrite by means of XAS. Results of our XAS experiment imply that the state of Au in pyrite is independent of the redox conditions: the local atomic environment of Au in pyrites formed in the oxidized system at 450 °C (H_2S/SO_2 couple controls the redox state) is similar to the one which corresponds to the reduced media at 300 °C (H_2S is the dominant form of sulfur).

Results of our study imply that the As-free pyrite can contain Au in the solid solution state at the 100 ppm level. This conclusion is in line with previous studies of Au sorption and precipitation with pyrite (c.f., Kozerenko et al., 2001; Widler and Seward, 2002; Laptev and Rozov, 2006), as well as with our study of the state of Au in synthetic As-free pyrite by XAS (Trigub et al., 2017a). Examination of the concentration of the "invisible" Au in pyrite (Table 1) confirms the results of XAS experiment and shows that Au and As behave independently during the pyrite-forming processes studied in the present work. Results of our study imply that the concentration of the solid solution Au is independent of the As content. For example, in the sample of natural arsenian pyrite from the Samolazovskoe Au-sulfide deposit (*C*(As) ~ 0.34 wt%) the concentration of "invisible" Au = 300 ppm only slightly exceeds the average Au content of ~200 ppm in low-temperature (300 °C) synthetic As-free pyrites. At the same time, analysis of the EXAFS spectra suggests that the natural arsenian pyrite can contain an admixture of Au_2S-like clusters along with the solid solution Au, which increases the "invisible" Au concentration. The concentration of "invisible" Au decreases twofold with the increase of the temperature from 300 to 450 °C: the average Au content in synthetic Au samples is ~200 ppm at 300 °C and < 100 ppm at 450 °C in Au-saturated system in the presence of Au metal. This result is consistent with analysis of natural Au-bearing pyrites from various deposit types (Deditius et al., 2014), as well as with our previous study (Trigub et al., 2017a) where it was demonstrated that increase of temperature results in decrease of the "invisible" Au concentration in pyrite from a few hundred ppm at ambient temperature to < 100 ppm at 300–500 °C. Similar retrograde behavior of the concentration of Au in synthetic As-free pyrites was observed in Pokrovski et al. (2019). Based on the results of theoretical modeling of Au L_3-edge HERFD-XANES spectra Pokrovski et al. (2019) suggested that the main form of the "invisible" Au in their pyrite samples were clusters of linear S-Au-S units similar to the aqueous sulfur-bearing complexes and Au_2S. However, Trigub et al. (2017a) demonstrated that, despite the fact that Au L_3-edge XANES spectra of Au_2S and the "invisible" Au in pyrite are close in shape and positions of the main spectral features, their direct comparison, as well as the theoretical modeling of the XANES spectra of Au-bearing pyrites, cannot produce unambiguous information on the state of Au. The analysis of Au L_3-edge XANES spectra should be complemented with EXAFS spectra modeling to unambiguously determine the state of Au in pyrite. It is possible that both the Au_2S-like clusters and the solid solution Au were present in the pyrite samples of Pokrovski et al. (2019).

In three experiments the solubility of Au dissolved in the hydrothermal fluid was determined along with the Au content in pyrite. These data indicate that As does not affect the hydrothermal transport of Au, at least at acidic pH imposed by the H_2S-SO_2 couple where the neutral species $H_3AsO_3^\circ$ predominates (Experiments No. 8 and 10 at 450 °C, Table 1). The measured Au concentrations are in close agreement with our data published previously (Trigub et al., 2017b) and are accounted for by the formation of $AuHS^\circ$ – the main form of Au in acidic sulfide-bearing fluids (c.f., Benning and Seward, 1996; Stefánsson and Seward, 2004; Tagirov et al., 2005). Jump-like increase of Au concentration observed in As-rich system (Experiment No. 16, 450 °C, Table 1) can be attributed to the contamination of the sample by the fluid phase with Au-rich amorphous As_2S_3 phase (which contains ca. 1 wt% Au) which was deposited during quenching and found on the autoclave walls after the experiment.

Arsenic in natural and synthetic samples of arsenian pyrites exists in 1−, 3+, and 5 + oxidation states. Natural pyrites contain mostly As^{1-} in the form of the solid solution when As substitutes for S in the pyrite anionic sites. The sample from the Samolazovskoe Au-sulfide deposit contains an admixture of $As_2^{3+}O_3$. The states of As in synthetic pyrites are more diverse. The samples contain As in the form of the solid solution As^{1-} along with As^{3+} and As^{5+} oxides. Besides, As can present in pyrite as a minor admixture of tiny inclusions of Au-bearing arsenopyrite or löllingite: we were not able to discriminate between these minerals. Despite oxidized redox state in several experimental systems traced by the presence of As oxides, no incorporation of As into octahedral cationic Fe sites, which was suggested in Le Pape et al. (2016), was observed in our study.

Savage et al. (2000) determined that in the sample of arsenian pyrite from tailings of the Clio Mine of the Mother Lode Gold District As substitutes for S with significant As-As clustering. By means of comparison of the Fourier transform (FT) of the experimental As *K*-edge EXAFS spectrum with the FTs of the spectra simulated theoretically the authors found the ~30% substitution of As for S in the nearest to As sites. Besides, the best fit of the experimental spectrum was achieved when ~43% of S atoms in the 2nd shell were substituted by As. Our study resulted in the 1st shell As-S and As-Fe distances (2.25–2.28 Å and 2.32–2.34 Å, correspondingly) which agree within the uncertainty with data of Savage et al. (2000). However, we did not observe a contribution from As in the 1st and 2nd shells around the excited As atom which implies insignificant As-As clustering in the studied samples.

An important issue of our work is that in the studied pyrite samples the states of As and Au are decoupled: the presence of As in the ore-forming system and its form of occurrence in pyrite has no effect on the speciation of Au which presents in the form of the solid solution Au or Au_2S-like clusters regardless of the state of As. We note, however, that in the present study the decoupling of As and Au chemistry is demonstrated only for synthetic pyrites and a sample from Au-sulfide deposit. In these samples the Au and As concentrations are not correlated. In contrast, in pyrites from the Carlin-type deposits strong positive Au vs. As correlation is observed (e.g., Fleet and Mumin, 1997; Reich et al., 2005; Deditius et al., 2014). In the light of our results, there are two possible explanations of this correlation. First, due to high As content, the As-As clustering can take place in As-rich pyrite grains or zones within the grains. The presence of the arsenopyrite or löllingite-like clusters/domains in the matrix of pyrite can greatly increase the concentration of Au (for example, the solid solution Au concentration can reach about 0.1 wt% in löllingite, Trigub et al., 2017a). Second, the formation of pyrites which are enriched in both Au and As can reflect the chemistry of the ore-forming fluids. In this case, the simultaneous increase of the concentrations of As and Au dissolved in the ore-forming fluid would result in the formation of Au-rich arsenian pyrites. We note, however, that additional spectroscopic experiments are necessary to reveal the state of Au in the ores of Carlin-type deposits.

5. Conclusions

The main purpose of this work was to determine the effect of physicochemical parameters and As concentration on the state of Au in pyrite. We obtained Au-bearing As-free and arsenian pyrites by means of hydrothermal technique. The synthesis experiments were performed

in the wide range of *T-P*-compositional parameters: at 300 °C/P_{sat} and 450 °C/1 kbar, in oxidized and reduced sulfide fluids, and in As-free and As-bearing systems. The synthesized pyrites contained up to 1.5 wt% As. Results of LA-ICP-MS chemical analyses showed that both Au and As are homogeneously distributed within the matrix of synthetic pyrite samples. The concentration of "invisible" Au in pyrite was found to be independent of the As content and varied between ca. 100 and 300 ppm. The concentration of Au dissolved in aqueous acidic sulfide fluid was also independent from the As content which implies that $AuHS^{\circ}$ complex was the dominant Au species at the experimental parameters. The retrograde behavior of the "invisible" Au in pyrite with respect to temperature was observed: the increase of the pyrite formation temperature resulted in a decrease of Au concentration. X-ray absorption spectroscopy (XAS) was applied to determine the local atomic environment and the valence state of Au and As in the synthesized pyrite samples, which were compared to the natural arsenian pyrite from the Samolazovskoe Au-sulfide deposit (Yakutia, Russia, the sample contained ca. 300 ppm Au and 0.34 wt% As). According to XANES spectra analysis, the "formal" oxidation state of "invisible" Au in all the samples is 1+. Two forms of "invisible" Au in pyrite were identified by means of the EXAFS spectra analysis. The first form is the solid solution Au, the second one is the Au_2S-like clusters/inclusions. In the solid solution state Au substitutes for Fe and is in octahedral coordination with S atoms independently of As content. The Me-S bond length in the first coordination shell increases from 2.26 Å of pure pyrite to 2.41 Å for Au-S bond. The distant coordination shells of the solid solution Au are similar to the pure pyrite structure. In some samples, the Au atoms were identified in the 2nd coordination shell of the excited Au atom which was interpreted as clustering of the solid solution Au. In these samples, the distant coordination shells are of disordered character. The presence of the second form, the Au_2S-like clusters, resulted in a significant decrease of the Au-S distance and coordination number (in Au_2S $R_{Au\text{-}S}$ = 2.30 Å and N_S = 2). In one sample of synthetic arsenian pyrite the As atoms were observed in the 2nd shell of Au and were attributed to the presence of Au-bearing arsenopyrite and/or löllingite. Accordingly, the presence of Au-bearing arsenopyrite and löllingite in the matrix of pyrite can increase the bulk concentration of Au and cause Au enrichment in natural arsenian pyrites. The oxidation state of As varied from 1− to 5+. The solid solution state, where As^{1-} substituted for S, was the dominant form of As in natural arsenian pyrites. In this case, due to the large ionic radius of As, the interatomic distances in the 1st shell increased from $R_{S\text{-}Fe}$ = 2.18 Å in pure pyrite to $R_{As\text{-}Fe}$ 2.25–2.28 Å in arsenian one. The 3+ and 5+ oxidation states were identified in synthetic pyrites and interpreted as the presence of As oxides. Analysis of XAS data demonstrated that the speciation of As and the redox state of the system do not affect the state of Au. Additional spectroscopy experiments are necessary to characterize the state of Au in As-rich ores of the Carlin-type deposits with the strong direct correlation between the concentrations of Au and As in pyrite.

Acknowledgements

The authors thank the ESRF for the beamtime allocation under the proposal No. ES-602 (BM16–FAME–UHD). We thank Vera Abramova and Dmitry Petrenko for the chemical analyses of synthesized minerals using LA-ICP-MS and ICP-MS methods, and Elena Bazarkina for insightful discussions. We are grateful to Laurent Truche for helpful reviews of the manuscript. Yan Mei is acknowledged for editorial handling. Chemical analyses were performed at the "IGEM-Analytica" Center for Collective Use. This study was supported by the Russian Science Foundation grant No. 20-17-00208 (synthetic phases) and the Russian Science Foundation grant No. 17-17-01220-P (natural minerals).

Appendix A. Supplementary data

Supplementary data to this article can be found online at https://doi.org/10.1016/j.oregeorev.2020.103475.

References

Belogub, E., Novoselov, K., Artem'ev, D., 2019. Impurities in pyrite from the gold deposits of Central Aldan ore area (Sakha-Yakutia, Russia): study using LA ICP-MS. Proceedings of the 15th Biennial SGA Meeting, Life with Ore Deposits on Earth, Glasgow, Extended Abstracts, 2, 818-822.

Benning, L.G., Seward, T.M., 1996. Hydrosulphide complexing of Au (I) in hydrothermal solutions from 150–400°C and 500–1500 bar. Geochim. Cosmochim. Acta 60, 1849–1871.

Bi, S.J., Li, J.W., Zhou, M.F., Li, Z.K., 2011. Gold distribution in As-deficient pyrite and telluride mineralogy of the Yangzhaiyu gold deposit, Xiaoqinling district, southern North China craton. Miner Depos. 46 (8), 925–941.

Bindi, L., Moelo, Y., Léone, P., Suchaud, M., 2012. Stoichiometric arsenopyrite, FeAsS, from La Roche-balue quarry, loire-atlantique, france: crystal structure and mössbauer study. Can. Mineral. 50 (2), 471–479.

Borisenko I. D., Borovikov A. A., Borisenko A. A., Gaskov I. V., Prokopiev I.R., 2015. Ore-Forming fluids of gold-porphyry and skarn deposits in Central-Aldan (Southern Yakutia) based on fluid inclusion study. Proceedings of the 13th Biennial SGA Meeting, Mineral Resources in a Sustainable World, Nancy, France, Extended Abstracts, 417–420.

Brostigen, G., Kjekshus, A., 1969. Redetermined Crystal Structure of FeS2 (Pyrite). Acta Chem. Scand. 23, 2186–2188.

Chareev, D.A., 2016. General principles of the synthesis of chalcogenides and pnictides in salt melts using a steady-state temperature gradient. Crystallogr. Rep. 61 (3), 506–511.

Chen, J.-H., Li, Y.-Q., Zhong, S.-P., 2013. DFT simulation of the occurrences and correlation of gold and arsenic in pyrite. Am. Mineral. 98 (10), 1765–1771.

Chen, L., Li, X., Li, J., Hofstra, A.H., Liu, Y., Koenig, A.E., 2015. Extreme variation of sulfur isotopic compositions in pyrite from the Qiuling sediment-hosted gold deposit, West Qinling orogen, central China: an in situ SIMS study with implications for the source of sulfur. Miner Depos. 50 (6), 643–656.

Chernyshov, A.A., Veligzhanin, A.A., Zubavichus, Y.V., 2009. Structural materials science end-station at the kurchatov synchrotron radiation source: recent instrumentation upgrades and experimental results. Nucl. Instrum. Meth. A 603 (1–2), 95–98.

Cook, N.J., Ciobanu, C.L., Mao, J., 2009. Textural control on gold distribution in As-free pyrite from the Dongping, Huangtuliang and Hougou gold deposits, North China Craton (Hebei Province, China). Chem. Geol. 264 (1–4), 101–121.

Dai, Y., Hughes, J.M., Moore, P.B., 1991. The crystal of mimetite and clinomimetite, Pb5(AsO4)3Cl. Can. Mineral. 29 (2), 369–376.

Deditius, A.P., Reich, M., Kesler, S.E., Utsunomiya, S., Chryssoulis, S.L., Walshe, J., Ewing, R.C., 2014. The coupled geochemistry of Au and As in pyrite from hydrothermal ore deposits. Geochim. Cosmochim. Acta 140, 644–670.

Fadeev, A.V., Kozerenko, S.V., 1999. Gold in processes of pyrite formation. Part 1. Gold accumulation during pyrite formation. Geochem. Int. 37 (12), 1182–1190.

Filimonova, O.N., Trigub, A.L., Tonkacheev, D.E., Nickolsky, M.S., Kvashnina, K.O., Chareev, D.A., Chaplygin, I.V., Kovalchuk, E.V., Sara, Lafuerza, Tagirov, B.R., 2019. Substitution mechanisms in In-, Au-, and Cu-bearing sphalerites studied by X-ray absorption spectroscopy of synthetic compounds and natural minerals. Mineral. Mag. 83 (3), 435–451.

Fleet, M.E., Chryssoulis, S.L., MacLean, P.J., Davidson, R., Weisener, C.G., 1993. Arsenian pyrite from gold deposits; Au and As distribution investigated by SIMS and EMP, and color staining and surface oxidation by XPS and LIMS. Can. Mineral. 31 (1), 1–17.

Fleet, M.E., Mumin, A.H., 1997. Gold-bearing arsenian pyrite and marcasite and arsenopyrite from Carlin Trend gold deposits and laboratory synthesis. Am. Mineral. 82 (1–2), 182–193.

Franchini, M., McFarlane, C., Maydagán, L., Reich, M., Lentz, D.R., Meinert, L., Bouhier, V., 2015. Trace metals in pyrite and marcasite from the Agua Rica porphyry-high sulfidation epithermal deposit, Catamarca, Argentina: textural features and metal zoning at the porphyry to epithermal transition. Ore Geol. Rev. 66, 366–387.

Genkin, A.D., Bortnikov, N.S., Cabri, L.J., Wagner, F.E., Stanley, C.J., Safonov, Y.G., McMahon, G., Friedl, J., Kerzin, A.L., Gamyanin, G.N., 1998. A multidisciplinary study of invisible gold in arsenopyrite from four mesothermal gold deposits in Siberia, Russian Federation. Econ. Geol. 93 (4), 463–487.

Glatzel, P., Bergman, U., 2005. High resolution 1s core hole X-ray spectroscopy in 3d transition metal complexes – electronic and structural information. Coord. Chem. Rev. 249, 65–95.

Goldfarb, R.J., Baker, T., Dube, B., Groves, D.I., Hart, C.J., Gosselin, P., 2005. Distribution, character and genesis of gold deposits inmetamorphic terranes, Economic Geology 100th Anniversary Volume, 407-450.

Groves, D.I., Goldfarb, R.J., Gebre-Mariam, M., Hagemann, S.G., Robert, F., 1998. Orogenic gold deposits: a proposed classification in the context of their crustal distribution and relationship to other gold deposit types. Ore Geol. Rev. 13, 7–27.

Ivanova, J.N., Tykova, E.E., Abramova, V.D., Kovalchuk, E.V., Vikentyev, I.V., André-Meyer, A.S., 2015. Ores mineralogy and first data about "invisible" form of Au in pyrite of the Novogodnee-Monto deposit (the Polar Urals, Russia), Proceedings of the 13th Biennial SGA Meeting, Mineral Resources in a Sustainable World, Nancy, France, Extended Abstracts, 121-125.

Kampf, A.R., Downs, R.T., Housley, R.M., Jenkins, R.A., Hyršl, J., 2011. Anorpiment, As2S3, the triclinic dimorph of orpiment. Mineral. Mag. 75 (6), 2857–2867.

Kampmann, T.C., Jansson, N.F., Stephens, M.B., Olin, P.H., Gilbert, S., Wanhainen, C., 2018. Syn-tectonic sulphide remobilization and trace element redistribution at the Falun pyritic Zn-Pb-Cu-(Au-Ag) sulphide deposit, Bergslagen, Sweden. Ore Geol. Rev. 96, 48–71.

Kitahama, K., Kiriyama, R., Baba, Y., 1975. Refinement of the crystal structure of scorodite. Acta Cryst. B 31 (1), 322–324.

Kovalchuk E.V., Tagirov B.R., Vikentyev I.V., Chareev D.A., Tyukova E.E., Nickolsky M.S., Borisovsky S.E., Bortnikov N.S., 2019. «Invisible» gold in synthetic and natural crystals of arsenopyrite (Vorontsovka deposit, North Ural) Geology of Ore Deposits 61 (5), in press.

Kozerenko, S.V., Wagner, F.E., Friedl, J., Fadeev, V.V., 2001. Gold in pyrite formation processes: 3. Mössbauer study of synthetic gold-bearing iron sulfides. Geochem. Int. 39 (suppl. 2), 167-172.

Laptev, Yu.V., Rozov, K.B., 2006. Interaction of gold with sulfide surface as a factor of its concentration in hydrothermal ore formation. Doklady Earth Sci. 411 (8), 1229–1232.

Large, R.R., Danyushevsky, L., Hollit, C., Maslennikov, V., Meffre, S., Gilbert, S., Bull, S., Scott, R., Emsbo, P., Thomas, H., Singh, B., Foster, J., 2009. Gold and trace element zonation in pyrite using a laser imaging technique: Implications for the timing of gold in orogenic and Carlin-style sediment-hosted deposits. Econ. Geol. 104 (5), 635–668.

Large, R.R., Maslennikov, V.V., Robert, F., Danyushevsky, L.V., Chang, Z., 2007. Multistage sedimentary and metamorphic origin of pyrite and gold in the Giant Sukhoi log deposit, Lena Gold Province, Russia. Econ Geol. 102 (7), 1233–1267.

Leistel, J.M., Marcoux, E., Deschamps, Y., Joubert, M., 1997. Antithetic behavior of gold in the volcanogenic massive sulphide deposits of the Iberian Pyrite Belt. Miner. Depos. 33 (1–2), 82–97.

Le Pape, P., Blanchard, M., Brest, J., Boulliard, J.C., Ikogou, M., Stetten, L., Wang, S., Landrot, G., Morin, G., 2016. Arsenic incorporation in pyrite at ambient temperature at both tetrahedral S-I and octahedral feii sites: evidence from EXAFS–DFT Analysis. Environ. Sci. Technol. 51 (1), 150–158.

Leontiev, V.I., Bushuev, Ya.Yu., Chernigovcev, K.A., 2018. Samolazovskoe gold deposit (Central Aldan ore district): geological structure and mineralization of deep horizons. Regional Geology and Metallogeny 75, 90-103 (in Russian).

Llorens, I., Lahera, E., Delnet, W., Proux, O., Braillard, A., Hazemann, J.-L., Prat, A., Testemale, D., Dermigny, Q., Gelebart, F., Morand, M., Shukla, A., Bardou, N., Ulrich, O., Arnaud, S., Berar, J.-F., Boudet, N., Caillot, B., Chaurand, P., Rose, J., Doelsch, E., Martin, P., Solari, P.L., 2012. High energy resolution five-crystal spectrometer for high quality fluorescence and absorption measurements on an x-ray absorption spectroscopy beamline. Rev. Sci. Instrum. 83 (6), 063104.

Mercier-Langevin, P., Hannington, M.D., Dubé, B., Bécu, V., 2011. The gold content of volcanogenic massive sulfide deposits. Miner. Depos. 46 (5–6), 509–539.

Merkulova, M., Mathon, O., Glatzel, P., Rovezzi, M., Batanova, V., Marion, P., Boiron, M.-C., Manceau, A., 2019. Revealing the Chemical Form of "Invisible" Gold in Natural Arsenian Pyrite and Arsenopyrite with High Energy-Resolution X-ray Absorption Spectroscopy. ACS Earth and Space Chem., published online.

Murzin, V.V., Naumov, E.A., Azovskova, O.B., Varlamov, D.A., Rovnushkin, M.Yu., Pirajno, F., 2017. The vorontsovskoe Au-Hg-As ore deposit (Northern Urals, Russia): geological setting, ore mineralogy, geochemistry, geochronology and genetic model. Ore Geol. Rev. 85, 271–298.

Newville, M., Carroll, S. A., O'day, P. A., Waychunas, G., Ebert, M., 1999. A web-based library of XAFS data on model compounds. J. Synchrotron Radiat. 6 (3), 276-277.

Palenik, C.S., Utsunomiya, S., Reich, M., Kesler, S.E., Wang, L., Ewing, R.C., 2004. "Invisible" gold revealed: direct imaging of gold nanoparticles in a Carlin-type deposit. Am. Mineral. 89 (10), 1359–1366.

Palenova, E.E., Belogub, E.V., Novoselov, K.A., Maslennikov, V.V., Kotlyarov, V.A., Blinov, I.A., Plotinskaya, O.Y., Griboedova, I.G., Kuzmenko, A.A., 2015. Chemical evolution of pyrite at the Kopylovsky and Kavkaz black shale-hosted gold deposits, Bodaybo district, Russia: evidence from EPMA and LA-ICP-MS data. Geol. Ore Depos. 57 (1), 64–84.

Pals, D.W., Spry, P.G., Chryssoulis, S., 2003. Invisible gold and tellurium in arsenic-rich pyrite from the Emperor gold deposit, Fiji: Implications for gold distribution and deposition. Econ. Geol. 98, 479–493.

Pertlik, F., 1978. Verfeinerung der Kristallstruktur des Minerals Claudetit, As2O3 ("Claudetit I"). Monatsh. Chem. 109 (2), 277–282.

Piña, R., Gervilla, F., Barnes, S.J., Oberthür, T., Lunar, R., 2016. Platinum-group element concentrations in pyrite from the Main Sulfide Zone of the Great Dyke of Zimbabwe. Miner. Depos. 51 (7), 853–872.

Pokrovski, G., Kokh, M., Proux, O., Hazemann, J.L., Bazarkina, E., Testemale, D., Escoda, C., Boiron, M.-C., Blanchard, M., Aigouy, T., Gouy, S., De Parseval, P., Thibaut, M., 2019. The nature and partitioning of invisible gold in the pyrite-fluid system. Ore Geol. Rev. 109, 545–563.

Proux, O., Lahera, E., Del Net, W., Kieffer, I., Rovezzi, M., Testemale, D., Irar, M., Thomas, S., Aguilar-Tapia, A., Bazarkina, E.F., Prat, A., Tella, M., Auffan, M., Rose, J., Hazemann, J.L., 2017. High-energy resolution fluorescence detected X-ray absorption spectroscopy: A powerful new structural tool in environmental biogeochemistry sciences. J. Environ. Qual. 46 (6), 1146–1157.

Ravel, B., Newville M., 2005. A.T.H.E.N.A. ATHENA, ARTEMIS, HEPHAESTUS: data analysis for X-ray absorption spectroscopy using IFEFFIT. J. Synchrotron Radiat. 12 (4), 537-541.

Reich, M., Kesler, S.E., Utsunomiya, S., Palenik, C.S., Chryssoulis, S.L., Ewing, R.C., 2005. Solubility of gold in arsenian pyrite. Geochim. Cosmochim. Acta 69 (11), 2781–2796.

Savage, K.S., Tingle, T.N., O'Day, P.A., Waychunas, G.A., Bird, D.K., 2000. Arsenic speciation in pyrite and secondary weathering phases, Mother Lode gold district, Tuolumne County, California. Appl. Geochem. 15 (8), 1219–1244.

Stefánsson, A., Seward, T.M., 2004. Gold(I) complexing in aqueous sulphide solutions to 500°C at 500 bar. Geochim. Cosmochim. Acta 68, 4121–4143.

Tagirov, B.R., Salvi, S., Schott, J., Baranova, N.N., 2005. Experimental study of gold-hydrosulphide complexing in aqueous solutions at 350–500°C, 500 and 1000 bars using mineral buffers. Geochim. Cosmochim. Acta 69, 2119–2132.

Tagirov, B.R., Baranova, N.N., Zotov, A.V., Schott, J., Bannykh, L.N., 2006. Experimental determination of the stabilities of Au_2S(cr) at 25° C and Au $(HS)_2^-$ at 25–250° C. Geochim. Cosmochim. Acta 70 (14), 3689–3701.

Tagirov, B.R., Trigub, A.L., Kvashnina, K.O., Shiryaev, A.A., Chareev, D.A., Nickolsky, M.S., Abramova, V.D., Kovalchuk, E.V., 2016. Covellite CuS as a matrix for "invisible" gold: X-ray spectroscopic study of the chemical state of Cu and Au in synthetic minerals. Geochim. Cosmochim. Acta 191, 58–69.

Trigub, A.L., Tagirov, B.R., Kvashnina, K.O., Lafuerza, S., Filimonova, O.N., Nickolsky, M.S., 2017a. Experimental determination of gold speciation in sulfide-rich hydrothermal fluids under a wide range of redox conditions. Chem. Geol. 471, 52–64.

Trigub, A.L., Tagirov, B.R., Kvashnina, K.O., Chareev, D.A., Nickolsky, M.S., Shiryaev, A.A., Baranova, N.N., Kovalchuk, E.V., Mokhov, A.V., 2017b. X-ray spectroscopy study of the chemical state of "invisible" Au in synthetic minerals in the Fe-As-S system. Am. Mineral. 102 (5), 1057–1065.

Tseluyko, A.S., Maslennikov, V.V., Ayupova, N., Maslennikova, S.P., Danyushevsky, L.V., 2019. Tellurium-bearing mineralization in clastic ores at the Yubileynoe copper massive sulfide deposit (Southern Urals). Geol. Ore Deposits 61 (2), 133–161.

Vikent'eva, O.V., Bortnikov, N.S., André-Meyer, A.S., 2015. The large Svetlinsk Au-Te deposit, South Urals: telluride mineralization for genetic reconstructions. Proceedings of the 13th Biennial SGA Meeting, Mineral Resources in a Sustainable World, Nancy, France, Extended Abstracts, 851–854.

Vikentyev, I.V., 2006. Precious metal and telluride mineralogy of large volcanic-hosted massive sulfide deposits in the Urals. Mineral. Petrol. 87, 305–326.

Vikentyev, I.V., 2015. Invisible and microscopic gold in pyrite: methods and new data for massive sulfide ores of the Urals. Geol. Ore Depos. 57 (4), 237–265.

Vikentyev, I.V., Mansurov, R.K., Ivanova, Y.N., Tyukova, E.E., Sobolev, I.D., Abramova, V.D., Vykhristenko, R.I., Trofimov, A.P., Khubanov, V.B., Groznova, E.O., Dvurechenskaya, S.S., Kryazhev, S.G., 2017. Porphyry-style Petropavlovskoe gold deposit, the Polar Urals: geological position, mineralogy, and formation conditions. Geol. Ore Depos. 59 (6), 482–520.

Vikentyev, I.V., Tyukova, E.E., Vikent'eva, O.V., Chugaev, A.V., Dubinina, E.O., Prokofiev, V.Y., Murzin, V.V., 2019. Vorontsovka Carlin-style gold deposit in the North Urals: mineralogy, fluid inclusion and isotope data for genetic model. Chem. Geol. 508, 144–166.

Wagner, T., Klemd, R., Wenzel, T., Mattsson, B., 2007. Gold upgrading in metamorphosed massive sulfide ore deposits: direct evidence from laser-ablation–inductively coupled plasma–mass spectrometry analysis of invisible gold. Geology 35 (9), 775–778.

Widler, A.M., Seward, T.M., 2002. The adsorption of gold (I) hydrosulphide complexes by iron sulphide surfaces. Geochim. Cosmochim. Acta 66, 383–402.

Wilson, S.A., Ridley, W.I., Koenig, A.E., 2002. Development of sulfide calibration standards for the laser ablation inductively-coupled plasma mass spectrometry technique. J. Anal. At. Spectrom. 17 (4), 406–409.

Zabinsky, S.I., Rehr, J.J., Ankudinov, A., Albers, R.C., Eller, M.J., 1995. Multiple-scattering calculations of X-ray-absorption spectra. Phys. Rev. B 52 (4), 2995.